DOI: 10.1109/JESTPE.2017.2783042

Publisher version: https://ieeexplore.ieee.org/document/8194844

Noninvasive Online Parametric Identification of Three-Phase AC Power Impedances to Assess the Stability of Grid-Tied Power Electronic Inverters in LV Networks

Antonino Riccobono, *Member, IEEE*, Markus Mirz, *Student Member, IEEE* and Antonello Monti, *Senior Member, IEEE*
Institute for Automation of Complex Power Systems
E.ON Energy Research Center, RWTH Aachen University
Aachen 52074, Germany
[ariccobono, mmirz, amonti]@ eonerc.rwth-aachen.de

***Abstract*—This paper presents a noninvasive online parametric identification of three-phase AC power impedances to assess small-signal stability of grid-tied inverter systems by using well-known impedance-ratio-based stability criteria. The identification technique is integrated into the control of an existing grid-tied inverter for the estimation of wide bandwidth AC grid impedances, on top of its original power conversion function. This is accomplished in practice by injecting a short-time small-signal Pseudo Random Binary Sequence (PRBS), a digital approximation of white noise which is wide bandwidth in nature, on the inverter control loop so that all frequencies of interest at the impedance measurement point can be excited at once. Then, digital processing is performed in the integrated control platform where the parametric AC grid impedance is extracted from the measurement of voltage and current over the length of PRBS injection. Moreover, a procedure on how to identify the output impedance of the inverter is deployed so that the parametric source and load impedances can be used to verify the system stability by means of the generalized Nyquist stability criterion. The technique is validated via Hardware In the Loop (HIL) real-time simulation. The present work focuses on the identification of balanced three-phase AC impedances in *dq* reference frame and a *dq* diagonal-dominant stability analysis which is typical of LV Distribution Grids.**

***Index Terms*—Impedance Measurement, Inverters, Power System Stability, Stability Analysis, Stability Criteria**

I. INTRODUCTION

The traditional AC Power System is transforming into a Power-Electronics-based AC Power System due to the deeper integration of Renewable Energy Sources (RESs) and loads through grid-connected feedback-controlled power electronic converters [1]-[3]. This transformation is schematically depicted in Fig. 1, representing an exemplary low-voltage (LV) radial feeder. In Fig. 1 (a), the traditional AC LV feeder is mainly a passive network because the majority of loads are either AC machines, resistive, or diode rectifiers, fed by the MV/LV transformer. In Fig. 1 (b), the counterpart Power Electronics AC LV feeder is an active network where inverters interface the distributed RESs and active rectifiers interface all the loads. In the situation of Fig. 1 (b), it is also envisioned that the MV/LV conversion will be taken by solid-state transformer technology [4].

As power electronics penetrates the AC grid, a new challenge is raising for both power electronic engineers and power systems engineers. This proliferation of grid-connected power electronics can have a destabilizing effect on the AC voltage due to interactions among grid-connected feedback-controlled power electronic converters and equivalent power grid impedances seen at the various Point of Common Couplings (PCCs) [5]-[11]. In the literature, this stability problem has been explained in two ways. The first explanation considers the destabilizing equivalent negative incremental resistance behaviors of output and input impedance of grid-connected feedback-controlled inverters and active rectifiers, respectively [8]-[10]. The second explanation considers the interaction of the grid-connected converters and their control loops. When plotting the impedances of each subsystems connected at the various PCCs, the interaction manifests itself as an impedance magnitude overlap over a certain frequency range. This impedance overlap may bring the system into instability [5]-[10].

Initially proposed for DC power distribution systems, such as the Middlebrook criterion [12] and its extensions [13],

This work extends previously presented work at COMPEL 2016.

impedance-ratio-based stability criteria have been proposed and widely used to study the small-signal stability of Power-Electronics-based AC Power Distribution Systems [5]-[11]. All these stability criteria are based on the minor loop gain concept, i.e. an impedance ratio at the source/load interface at the PCC. Considering that the minor loop gain is a type of loop gain of an equivalent negative feedback loop system, the stability study can be performed by applying the Nyquist stability criterion to such a minor loop gain. AC impedances of balanced three-phase systems are usually represented in *dq* reference frame and are 2×2 matrixes[1]. Therefore, the impedance ratio, i.e. the minor loop gain, is also a 2×2 matrix. To study the stability of Power-Electronics-based AC Power Distribution Systems in *dq* domain, the generalized Nyquist stability criterion is used [8]-[11].

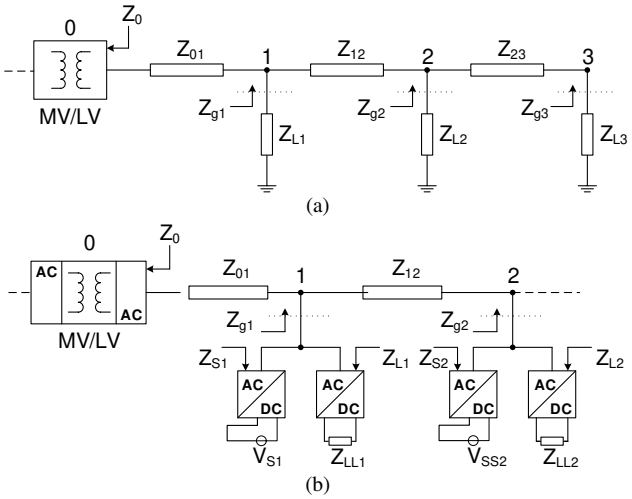

Fig. 1. Exemplary traditional passive LV radial feeder (a), and counterpart power electronics based feeder (b).

In order to apply the impedance-ratio-based stability criteria, it is necessary to know the interface impedances. Offline analytical methods to study the stability of Power-Electronics-based AC Power Distribution Systems are not enough because practically the system impedances continuously vary over time and in relation to too many parameters. Therefore, online methods to measure impedances are required in order to monitor system stability in real time and take corrective actions if needed. The ideal impedance measurement technique would complete the measurement in a short time, allowing fast response to system variations. Even though narrowband identification methods based on injection of sine sweeps give the best impedance measurement accuracy, they are not suitable for online applications due to the very long measurement times. In contrast, wideband identification methods based on injection of a high-frequency content signal able to excite all frequencies of interest simultaneously meet the requirement of fast measurement and have been proposed in the literature to measure impedances [14]-[31]. These methods were first proposed for DC systems [14]-[15], and then extended to AC systems [16]-[31]. These methods consist in generating a wideband perturbation controlled in both magnitude and duration for both voltage and current at the impedance measurement point. Then, advanced digital signal processing techniques can be applied on the measured voltage and current to identify the impedance of the system under test. The online wideband impedance identification methods can be categorized in steady-state methods and transient methods. In the steady-state methods, a wideband small-signal perturbation signal is superimposed onto the steady-state operating point for a certain amount of time and the impedance is extracted from the response during the perturbation [16]-[22],[24]. In the transient methods, usually a current impulse is injected at impedance measuring point and the impedance is extracted from its transient response [25],[29]-[30]. Despites the relatively longer perturbation, steady-state methods are recently of greater interest because of the too aggressive nature of the transient methods. The online wideband impedance identification methods can be further categorized in invasive methods [23]-[31], which require a dedicated power hardware to perform the impedance identification task, and noninvasive methods [14]-[22], which use the existing power hardware in the system. Among the noninvasive solutions, methods for wideband identification of power impedances in conjunction with existing power electronics converters are quite attractive, especially in Power-Electronics-based AC Power Distribution Systems [16]-[22]. In fact, since many of the converters connected to the AC grid have digital control and sensing, they may also be used to monitor AC power grid impedances on the top of their power conversion function. Digital network analyzer techniques [14]-[15] can be integrated into the converter controllers allowing them to be used as online monitors without any extra power hardware.

This paper presents an online wideband impedance identification method, called the Wideband System Identification (WSI) technique, which allows the integration of the control platform, where the WSI technique is implemented, into the controller of an existing grid-connected power electronic converter. More in the detail, the identification technique consists of injecting a short-time small-signal approximation of white noise (wide bandwidth in nature), i.e. Pseudo Random Binary Sequence (PRBS), on the control loop of the existing grid-connected power electronic converter while it is performing its power conversion function. Then, digital processing is performed in the integrated control platform to identify the grid impedance, i.e. the load subsystem impedance, in *dq* reference frame at the PCC from the voltage and current measurements over the length of the injection. The online WSI technique belongs to the category of the steady-state identification methods because PRBS is injected during the steady-state operation of the system. It also belongs to the category of noninvasive methods because it does not require any extra power hardware to inject the perturbation and measure voltages and currents needed to identify the impedance of the system under test.

With respect to past publications in the field of wideband measurement of AC grid impedances via existing grid-connected power electronic inverters [16]-[18], the new contribution of the present work resides in the implementation of the online parametrization of the identified non-parametric

[1] AC impedances can be modeled with other methods, such as harmonic linearization or modeling in the phase sequence domain, modeling with dynamic phasors, and reduced-order modeling [46],[47]. These methods are not object of this paper, but considerations for their usage are made in Section VII.

impedances in the same control platform. This allows the identification of parametric grid impedances in real time. The real-time parametrization of identified impedances is the key enabler for several system-level applications, such as online stability monitoring, harmonic propagation detection, active filter tuning, and adaptive control. Moreover, with respect to pure nonparametric identification, the authors envision that real-time parametrization of grid impedances will enable fast and reliable communication links for the system-level applications listed above at all automation levels of future Power-Electronics-based AC Power System such as that depicted in Fig. 1 (b). With respect to previously presented work by the authors [19], where the identification focused on the phase domain, this paper presents the online parametrization of the identified grid impedance in *dq* domain. Real-time parametric identification was recently presented by the authors [20], but with the different goal of improving stability and accuracy of a Power Hardware in the Loop setup and only considering passive DC impedances. This paper extends the identification to three-phase AC impedances. References [21]-[22] also used PRBS as perturbation signal and the impedance of the system under test was also identified in *dq* domain. However, they did not embody any parametric impedance identification in real time. Moreover, again with respect to [19], the procedure described in [21] to identify the parametric output impedance of the inverter is used, but parametric identification is embodied. Both the parametric inverter output impedance and grid impedance serve for small-signal stability analysis of grid-tied inverter systems by applying the generalized Nyquist stability criterion to the minor loop gain defined as the impedance ratio at the inverter/grid interface. The technique is verified in a Hardware In the Loop (HIL) real-time simulation setup. The HIL setup features an exemplary plant consisting of a grid-tied digitally-controlled inverter simulated in a real-time simulator and the digital platform where the identification algorithms are implemented.

The paper is organized as follows. Section II gives the theoretical background for stability analysis of grid-tied inverter systems. Section III derives analytic expressions for both the inverter output impedance and grid impedance in *dq* domain that will be the references which the results of the online WSI are compared to. Section IV presents the WSI technique and explains the methods for identification of both the grid impedance and the inverter output impedance in *dq* domain. Section V presents the HIL setup providing detailed description of all the routines and algorithms needed to online identify AC power impedances. Section VI gives the results of the online parametric impedance identification and stability analysis. Conclusions and future work are finally given in Section VII

II. Small-Signal Stability Analysis of Grid-Tied Inverter Systems

As an extension of the case for DC systems [12]-[13], impedance-ratio-based stability analysis for balanced three-phase systems is performed in this paper in the *dq* rotating frame to circumvent the modeling problem given by the time-variant nature of AC systems [8]-[11]. By applying a synchronous reference frame transformation to the measured quantities in the *abc* phase domain, the AC system becomes a multiple-input and multiple-output (MIMO) DC system in the *dq* domain. To derive the small-signal impedances in the *dq* domain, linearization techniques are used [37]. In *dq* domain, the obtained source and load AC impedances are the 2×2 matrixes (1) and (2), which clearly also have cross terms between the *d*-component and *q*-component.

$$\boldsymbol{Z_{S\_dq}}(s) = \begin{bmatrix} Z_{S\_dd}(s) & Z_{S\_dq}(s) \\ Z_{S\_qd}(s) & Z_{S\_qq}(s) \end{bmatrix} \quad (1)$$

$$\boldsymbol{Z_{L\_dq}}(s) = \begin{bmatrix} Z_{L\_dd}(s) & Z_{L\_dq}(s) \\ Z_{L\_qd}(s) & Z_{L\_qq}(s) \end{bmatrix} \quad (2)$$

The source-load system and its equivalent control block diagram are shown in Fig. 2.

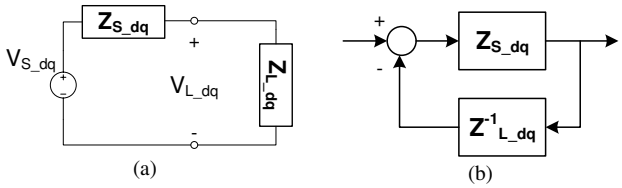

Fig. 2. Small-signal representation of a three-phase system in the *dq* domain (a), and equivalent MIMO feedback block diagram (b).

The source and load voltage vectors are defined as follows.

$$V_{S\_dq}(s) = \begin{bmatrix} v_{S\_d} \\ v_{S\_q} \end{bmatrix} \quad (3)$$

$$V_{L\_dq}(s) = \begin{bmatrix} v_{L\_d} \\ v_{L\_q} \end{bmatrix} \quad (4)$$

By inspection of Fig. 2, the load voltage can be calculated as follows.

$$V_{L\_qd}(s) = \left(\boldsymbol{I} + \boldsymbol{Z_{S\_dq}}(s) \cdot \boldsymbol{Z_{L\_dq}^{-1}}(s)\right)^{-1} \cdot V_{S\_dq}(s) \quad (5)$$

As a consequence, the so-called minor loop gain is given by

$$\boldsymbol{T_{MLG\_dq}}(s) = \boldsymbol{Z_{S\_dq}}(s) \cdot \boldsymbol{Z_{L\_dq}^{-1}}(s) = \boldsymbol{Z_{S\_dq}}(s) \cdot \boldsymbol{Y_{L\_dq}}(s) \quad (6)$$

where $\boldsymbol{Y_{L\_dq}}(s) = \boldsymbol{Z_{L\_dq}^{-1}}(s)$ is the load admittance matrix.

Using (1) and (2) in (6), the expression of the minor loop gain can be expanded as follows.

$$\boldsymbol{T_{MLG\_dq}}(s) = \boldsymbol{Z_{S\_dq}}(s) \cdot \boldsymbol{Y_{L\_dq}}(s) = \begin{bmatrix} Z_{S\_dd}(s) & Z_{S\_dq}(s) \\ Z_{S\_qd}(s) & Z_{S\_qq}(s) \end{bmatrix} \cdot \begin{bmatrix} Y_{L\_dd}(s) & Y_{L\_dq}(s) \\ Y_{L\_qd}(s) & Y_{L\_qq}(s) \end{bmatrix} = \begin{bmatrix} Z_{S_{dd}}(s)Y_{L_{dd}}(s) + Z_{S\_dq}(s)Y_{L\_qd}(s) & Z_{S_{dd}}(s)Y_{L_{dq}}(s) + Z_{S\_dq}(s)Y_{L\_qq}(s) \\ Z_{S_{qd}}(s)Y_{L_{dd}}(s) + Z_{S\_qq}(s)Y_{L\_qd}(s) & Z_{S_{qd}}(s)Y_{L_{dq}}(s) + Z_{S\_qq}(s)Y_{L\_qq}(s) \end{bmatrix} \quad (7)$$

Assuming stand-alone stability of the source and load subsystems, the interconnected three-phase system is stable if and only if the minor loop gain (7) satisfies the generalized Nyquist stability criterion. The reader can refer to [8]-[11] for its detailed formulation. In practice, the interconnected three-phase system is stable if and only if the Nyquist contours of the minor loop gain (7) do not encircle the $(-1, j0)$ point. Based on the concept of avoiding encircling the $(-1, j0)$ point in the complex plane, many impedance-ratio-based stability criteria were proposed for interconnected DC Power Systems and they are reviewed in [13]. They provide only sufficient, but not necessary stability conditions by defining various forbidden regions for the polar plot of the minor loop gain, defined at the power interface between source and load subsystems. The concept of forbidden regions perfectly applies to three-phase AC systems to derive design formulations for a stable interconnected system as demonstrated in [10].

To perform small-signal stability analysis of grid-connected

inverter systems, the classical approach consists in studying the linearized system under steady state conditions by assuming this convention: the grid-tied inverter is the source subsystem (subscript "S") and the grid is the load subsystem (subscript "G"), both connected at the PCC interface. Fig. 3 shows the equivalent system broken down into the two subsystems assumed to be individually stable. The inverter normally operates in current mode (Fig. 3 (a)); however, it can also operate in voltage mode (Fig. 3 (b)) to provide voltage support in case of an islanded microgrid formation or the main grid becomes weak [36].

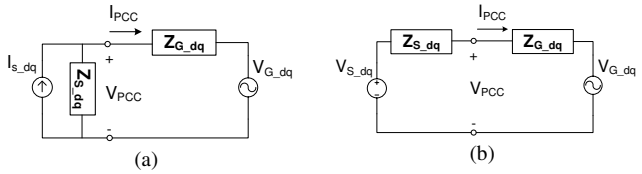

Fig. 3. Small-signal representation of the grid-tied inverter system in the *dq* domain. Inverter acting as a current source (a) and as voltage source (b).

Using the approach in [11], for the inverter operating in current mode (Fig. 3 (a)), the voltage at the PCC is

$$\begin{aligned} V_{PCC\_dq}(s) = &\left(\boldsymbol{Z_{S\_dq}^{-1}}(s) + \boldsymbol{Z_{G\_dq}^{-1}}(s)\right)^{-1} I_{S\_dq}(s) \\ &+ \boldsymbol{Z_{S\_dq}}(s) \\ &\cdot \left(\boldsymbol{Z_{S\_dq}}(s) + \boldsymbol{Z_{G\_dq}}(s)\right)^{-1} V_{G\_dq}(s) = \\ \left(\boldsymbol{I} + \boldsymbol{Z_{S\_dq}}(s)\boldsymbol{Z_{G\_dq}^{-1}}(s)\right)^{-1} &\cdot \boldsymbol{Z_{S\_dq}}(s) \cdot I_{S\_dq}(s) \\ &+ \left(\boldsymbol{I} + \boldsymbol{Z_{S\_dq}}(s)\boldsymbol{Z_{G\_dq}^{-1}}(s)\right)^{-1} \cdot V_{G\_dq}(s) \end{aligned} \quad (8)$$

where two minor loop gains are identifiable as follows

$$\boldsymbol{T_{MLG\_dq\_1}}(s) = \boldsymbol{Z_{S\_dq}}(s)\boldsymbol{Z_{G\_dq}^{-1}}(s) \quad (9)$$

$$\boldsymbol{T_{MLG\_dq\_2}}(s) = \boldsymbol{Z_{G\_dq}}(s)\boldsymbol{Z_{S\_dq}^{-1}}(s) \quad (10)$$

Being $\boldsymbol{T_{MLG\_dq\_1}}(s)$ the inverse matrix of $\boldsymbol{T_{MLG\_dq\_2}}(s)$, for the case of inverter operating in current mode it is demonstrated in [11] that applying the generalized Nyquist stability criterion to $\boldsymbol{T_{MLG\_dq\_2}}(s)$ is equivalent to apply the generalized inverse Nyquist stability criterion to $\boldsymbol{T_{MLG\_dq\_2}}(s)$ and to apply the generalized Nyquist criterion to $\boldsymbol{T_{MLG\_dq\_1}}(s)$. In practice, it is sufficient to apply the generalized Nyquist stability criterion to $\boldsymbol{T_{MLG\_dq\_2}}(s)$ or the more conservative criteria to avoid encirclement of the $(-1, j0)$ point [8].

Again using the approach in [11], for the inverter operating in voltage mode (Fig. 3 (b)), the voltage at the PCC is

$$\begin{aligned} V_{PCC\_dq}(s) = &\boldsymbol{Z_{G\_dq}}(s) \cdot \left(\boldsymbol{Z_{S\_dq}}(s) + \boldsymbol{Z_{G\_dq}}(s)\right)^{-1} V_{S\_dq}(s) \\ &+ \boldsymbol{Z_{S\_dq}}(s) \\ &\cdot \left(\boldsymbol{Z_{S\_dq}}(s) + \boldsymbol{Z_{G\_dq}}(s)\right)^{-1} V_{G\_dq}(s) = \\ \left(\boldsymbol{I} + \boldsymbol{Z_{S\_dq}}(s)\boldsymbol{Z_{G\_dq}^{-1}}(s)\right)^{-1} &\cdot V_{S\_dq}(s) \\ &+ \left(\boldsymbol{I} + \boldsymbol{Z_{G\_dq}}(s)\boldsymbol{Z_{S\_dq}^{-1}}(s)\right)^{-1} \\ &\cdot V_{G\_dq}(s) \end{aligned} \quad (11)$$

where the same two minor loop gains as defined in (9) and (10) are identifiable. For the case of inverter operating in voltage mode, the same relationship between generalized Nyquist stability criterion and generalized inverse Nyquist stability criterion applied to either $\boldsymbol{T_{MLG\_dq\_1}}(s)$ or $\boldsymbol{T_{MLG\_dq\_2}}(s)$ exist. In practice, it is convenient to apply the generalized Nyquist stability criterion to $\boldsymbol{T_{MLG\_dq\_1}}(s)$ or the more conservative criteria to avoid encirclement of the $(-1, j0)$ point [10].

Differently from DC systems which are single-input and single-output (SISO) systems, studying the stability of three-phase AC systems by using the generalized Nyquist stability criterion applied to the minor loop gains $\boldsymbol{T_{MLG\_dq\_1}}(s)$ or $\boldsymbol{T_{MLG\_dq\_2}}(s)$ can be very difficult and unpractical due to its MIMO nature. However, in LV Distribution Grids, simplifications can be obtained to at least obtain a diagonal-dominant matrix. In fact, if the LV power-electronics-based AC power system of Fig. 1 (b) is considered, then the cross terms of $\boldsymbol{T_{MLG\_dq\_1}}(s)$ and $\boldsymbol{T_{MLG\_dq\_2}}(s)$, defined at the various PCCs of the same system, can be neglected for the following two reasons:

- LV Distribution Grids are mainly resistive, i.e. $X/R < 1$ (negligible capacitive and inductive effects).
- Grid-connected inverters embody decoupling controls which significantly reduce the magnitude of the cross terms of their output impedance compared with the terms of the main diagonal [8].
- Grid-connected active rectifiers operate as high power factor loads and, as results, the magnitude of the cross terms of their input admittance is significantly reduced with respect to that of the terms of the main diagonal [10],[41].

Under this assumptions, the minor loop gains $\boldsymbol{T_{MLG\_dq\_2}}(s)$ or $\boldsymbol{T_{MLG\_dq\_1}}(s)$ used for stability analysis of grid-connected current-controlled and voltage-controlled inverter systems, respectively, can be simplified as (12) and (13).

$$\begin{aligned} &\boldsymbol{T_{MLG\_dq\_2}}(s) = \boldsymbol{Z_{G\_dq}}(s) \cdot \boldsymbol{Z_{S\_dq}^{-1}}(s) = \\ &\boldsymbol{Z_{G\_dq}}(s) \cdot \boldsymbol{Y_{S\_dq}}(s) \approx \\ &\begin{bmatrix} Z_{G\_dd}(s) & 0 \\ 0 & Z_{G\_qq}(s) \end{bmatrix} \cdot \begin{bmatrix} Y_{S\_dd}(s) & 0 \\ 0 & Y_{S\_qq}(s) \end{bmatrix} = \\ &\begin{bmatrix} Z_{G_{dd}}(s)Y_{S_{dd}}(s) & 0 \\ 0 & Z_{G\_qq}(s)Y_{S\_qq}(s) \end{bmatrix} \end{aligned} \quad (12)$$

$$\begin{aligned} &\boldsymbol{T_{MLG\_dq\_1}}(s) = \boldsymbol{Z_{S\_dq}}(s) \cdot \boldsymbol{Z_{G\_dq}^{-1}}(s) = \\ &\boldsymbol{Z_{S\_dq}}(s) \cdot \boldsymbol{Y_{G\_dq}}(s) \approx \\ &\begin{bmatrix} Z_{S\_dd}(s) & 0 \\ 0 & Z_{S\_qq}(s) \end{bmatrix} \cdot \begin{bmatrix} Y_{G\_dd}(s) & 0 \\ 0 & Y_{G\_qq}(s) \end{bmatrix} = \\ &\begin{bmatrix} Z_{S_{dd}}(s)Y_{G_{dd}}(s) & 0 \\ 0 & Z_{S\_qq}(s)Y_{G\_qq}(s) \end{bmatrix} \end{aligned} \quad (13)$$

Therefore, according to the simplifications in (12) and (13), small-signal stability analysis of the grid-tied inverter system requires the parametric identification of only four interface impedances, i.e. $Z_{S\_dd}(s), Z_{S\_qq}(s), Z_{G\_dd}(s)$, and $Z_{G\_qq}(s)$. These impedances are online identified through the WSI tool described in the Section V.

III. Impedance Modeling of Grid-Tied Inverters and Grid Impedances

The system under consideration is shown in Fig. 4 and consists of a feedback-controlled inverter connected to a lumped grid model. In this section the analytic expressions for both grid-tied inverter output impedance Z_{S_dq} and grid impedance Z_{G_dq} are given in *dq* reference frame and they will

be compared to the results of the identification in Section VI.

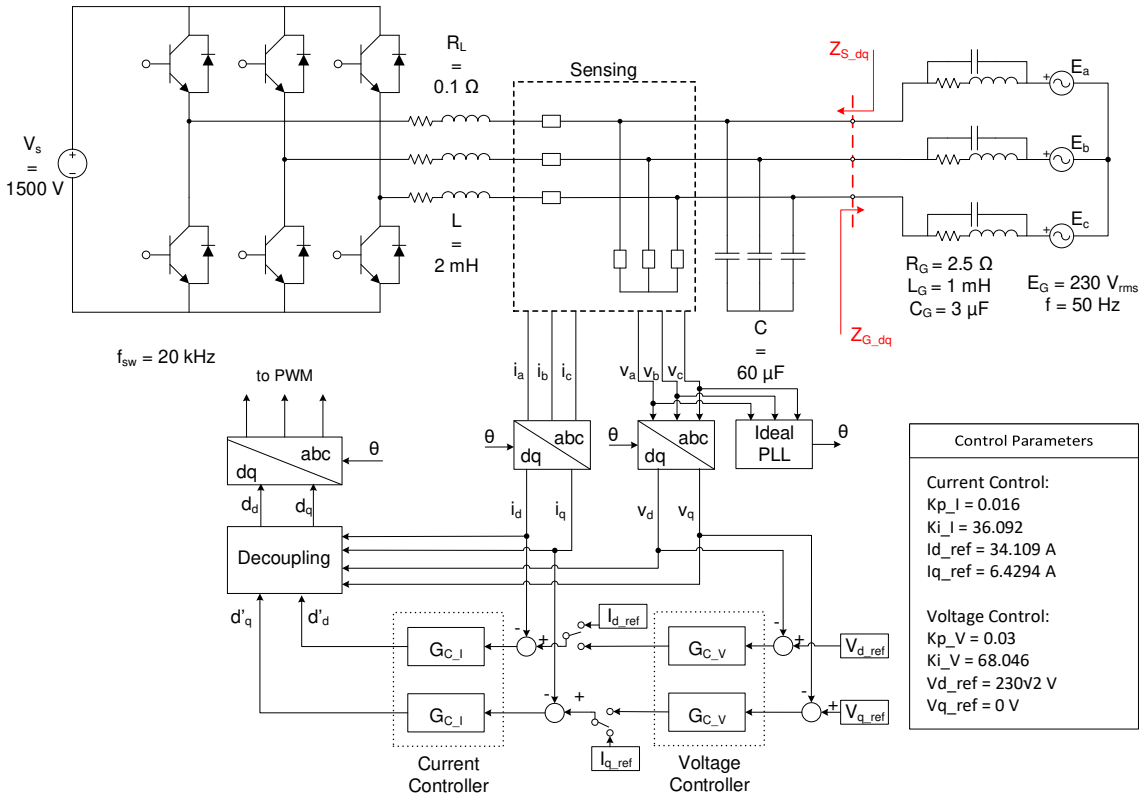

Fig. 4. Circuital diagram of the feedback-controlled inverter connected to a lumped grid model.

The circuital parameters of the three-phase inverter are reported in the same Fig. 4 along with its control parameters. The inverter, whose switching frequency is 20 kHz, is connected to a simplified balanced three-phase representation of the AC system consisting of an ideal three-phase voltage source E_{abc} and an equivalent linear Thévenin impedance Z_G modeled as Y-connected configuration as depicted in Fig. 4, whose circuital parameter values are also given. The controller consists of an inner current loop and an optional outer voltage loop and it is designed on a synchronous *dq* reference frame. The inverter normally operates in current mode to inject a certain amount of active (and reactive) power into the grid; however, it can also operate in voltage mode to provide voltage support in case of a microgrid formation [36]. The values of the *abc* duty cycles vary sinusoidally in synchronism with the AC grid voltage thanks to the use of an ideal Phase Locked Loop (PLL) (see again Fig. 4).

A. *Inverter Output Impedance*

In this paper, "Ideal PLL" means that its dynamics are neglected. In other words, an oscillator perfectly synchronized to the AC grid voltage is used. Inspired by [8], the authors are currently working on the derivation of a modeling framework in *dq* domain of grid-connected power electronic converters with real PLLs. By neglecting the dynamics of the PLL, the small-signal modeling is derived from the equivalent averaged model in *dq* rotating coordinates that is obtained from the averaged *abc*-model of the grid-connected inverter by using the Park Transformation. The first step of this procedure yields the open-loop large-signal averaged equations:

$$L\frac{di_d}{dt} = d_d v_s - v_d + \omega L i_q - R_L i_d \tag{14}$$

$$L\frac{di_q}{dt} = d_q v_s - v_q - \omega L i_d - R_L i_d \tag{15}$$

$$C\frac{dv_d}{dt} = i_d + \omega C v_q - i_{load\_d} \tag{16}$$

$$C\frac{dv_q}{dt} = i_q - \omega C v_d - i_{load\_q} \tag{17}$$

where v_d, v_q, i_d, i_q are the output voltage and inductor current state variables, respectively, and d_d, d_q are the control input variables. The currents i_{load_d} and i_{load_q} are the load currents.

The averaged model given by (14)-(17) contains cross-coupling terms between the *d* and *q* channels. In this paper, the decoupling technique of [40] is used to minimize the effect of the cross-coupling terms in the model. The small-signal open-loop model is derived by *perturbation-and-linearization* technique [37]. Then, the current and voltage controls are designed based on this small-signal model with the performance given in Table I.

TABLE I. INVERTER CONTROL PERFORMANCE

	Current Control	Voltage Control
Crossover Frequency (f_c)	2 kHz	100 Hz
Phase Margin (*PM*)	80°	80°

The inverter output impedance Z_{S_dq} in *dq* reference frame is derived under the influence of the current control and under the

influence of the voltage control. In this paper, a simulation modeling exercise is presented to derive such small-signal closed-loop models. This exercise not only will produce the analytic transfer functions which the results of the WSI technique will be compared to in Section VI, but also it will serve as validation tool for the ongoing modeling framework in *dq* domain of grid-connected power electronic converters with real PLLs. First, the averaged model of the inverter (14)-(15) with the feedback control was implemented in Simulink as depicted in Fig. 5. By performing a linear analysis in the "Control Design" toolbox in Simulink, it is possible to linearize the feedback-controlled averaged model of the inverter around an operating steady-state point by specifying linearization inputs and outputs and eventually extract transfer functions [43]. To extract the inverter output impedance, the linearization inputs are i_{load_d} and i_{load_q}, while the linearization outputs are v_d and v_q. The extracted analytic expressions of the inverter output impedances are reported in Appendix. These transfer functions are plotted in Fig. 6. Notice that when the dynamics of the PLL are neglected, the output characteristics of the inverter resemble like those of an uninterruptible power supply [42]. In fact, the components Z_{dd} and Z_{qq} are the same; the components Z_{dq} and Z_{qd} have also the same magnitude, but a phase shift of 180°. Moreover, the *dq* and *qd* components have a significant smaller magnitude compared to that of the *dd* and *qq* components. This shows that Z_{S_dq} can be considered to be diagonal dominant.

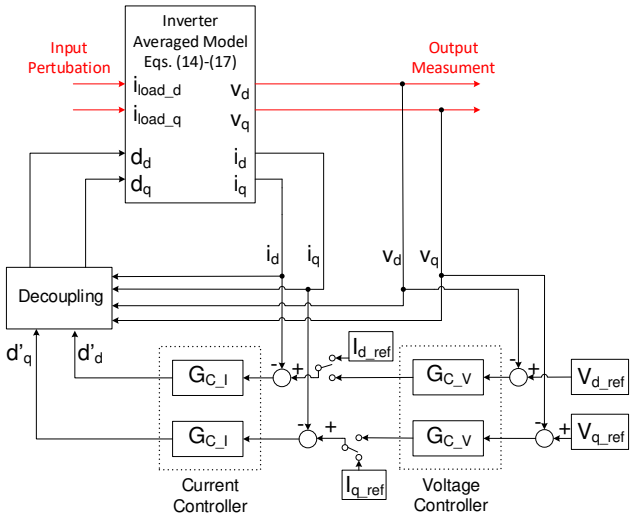

Fig. 5. Averaged model of the feedback-controlled inverter with signals highlighted in red to extract the inverter output impedance.

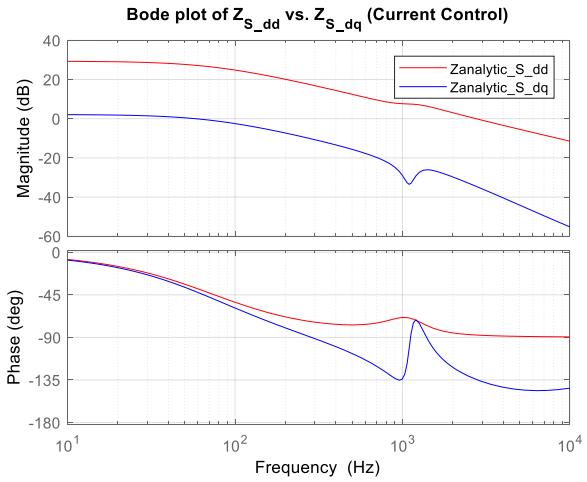

(a)

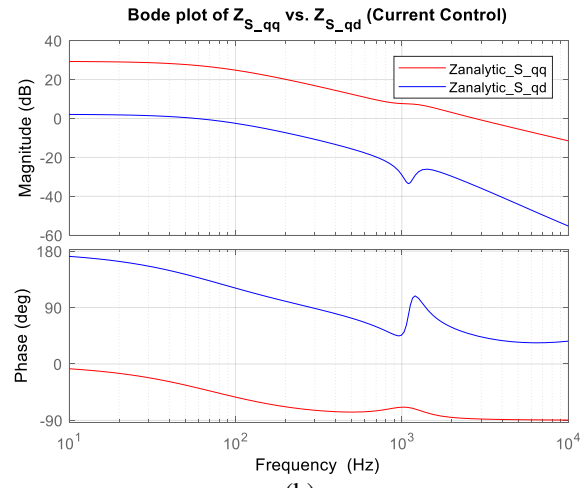

(b)

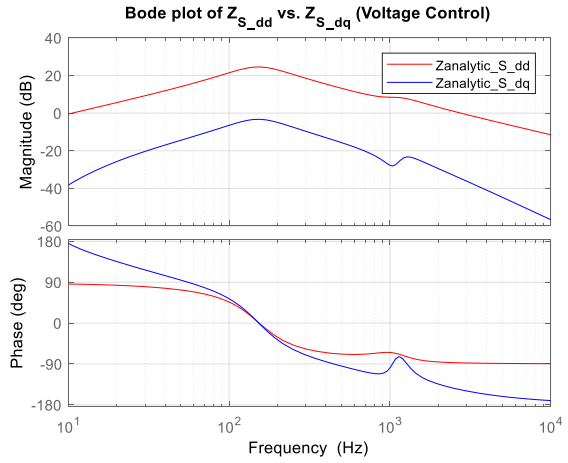

(c)

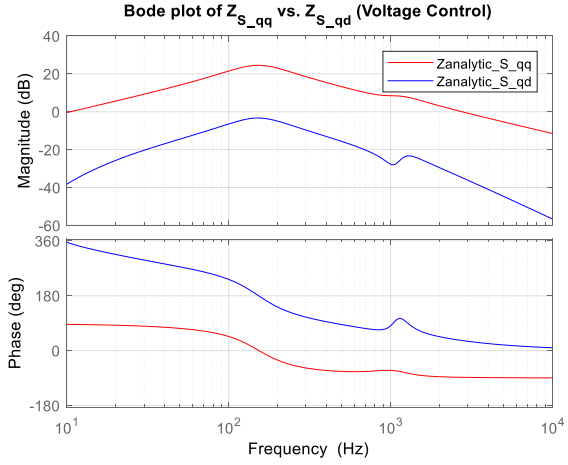

(d)

Fig. 6. Analytic output impedance of the inverter under current control (a)-(b), and voltage control (c)-(d).

B. Grid Impedance

In this paper, the grid impedance is modeled as a balanced three-phase RLC impedance as depicted at the right hand side of Fig. 4. An RL branch is in parallel to a capacitive branch. The equivalent grid impedance model in *dq* reference frame can be calculated as follows. The RL branch impedance in *dq* coordinates is given by

$$Z_{RL\_dq} = \begin{bmatrix} sL_G + R_G & -\omega_G L_G \\ \omega_G L_G & sL_G + R_G \end{bmatrix} \quad (18)$$

where ω_G is the AC system fundamental frequency, i.e. $2 \cdot \pi \cdot 50\, rad/s$. The capacitive branch admittance in *dq* coordinates is given by

$$Y_{C\_dq} = Z_{C\_dq}^{-1} = \begin{bmatrix} sC_G & -\omega_G C_G \\ \omega_G C_G & sC_G \end{bmatrix} \quad (19)$$

Finally, the RLC grid impedance in *dq* coordinates is calculated as follows.

$$Z_{G\_dq} = (Z_{RL}^{-1} + Z_C^{-1})^{-1} \quad (20)$$

Analytic expressions of the grid impedance can be calculated from (18) to (20) and can be found in Appendix. Two cases are under consideration, namely Case 1 and Case 2 whose circuital parameters are given in Table II. When the inverter is connected to the grid impedance labeled as Case 1, the system results in a more robustly stable fashion with respect to those of Case 2, as it will be shown in Section VI. These transfer functions are plotted in Fig. 7. Likewise, for the inverter output impedance, the components Z_{dd} and Z_{qq} are the same; the components Z_{dq} and Z_{qd} have also the same magnitude, but a phase shift of 180°. Moreover, the grid impedance can be surely considered as diagonal dominant for Case 1 because the magnitude of the *dd* (and *qq*) component is sufficiently larger than the magnitude of the *dq* (and *qd*) component for all frequencies. The grid impedance for Case 2 can be still considered diagonal dominant because the diagonal elements are sufficiently larger than the cross terms for all the frequencies except around and below the fundamental frequency.

TABLE II. GRID IMPEDANCE PARAMETERS FOR CASE 1 AND CASE 2

	Case 1	Case 2
R_G	2.5 Ω	1.2 Ω
L_G	1 mH	5 mH
C_G	3 μF	5 μF

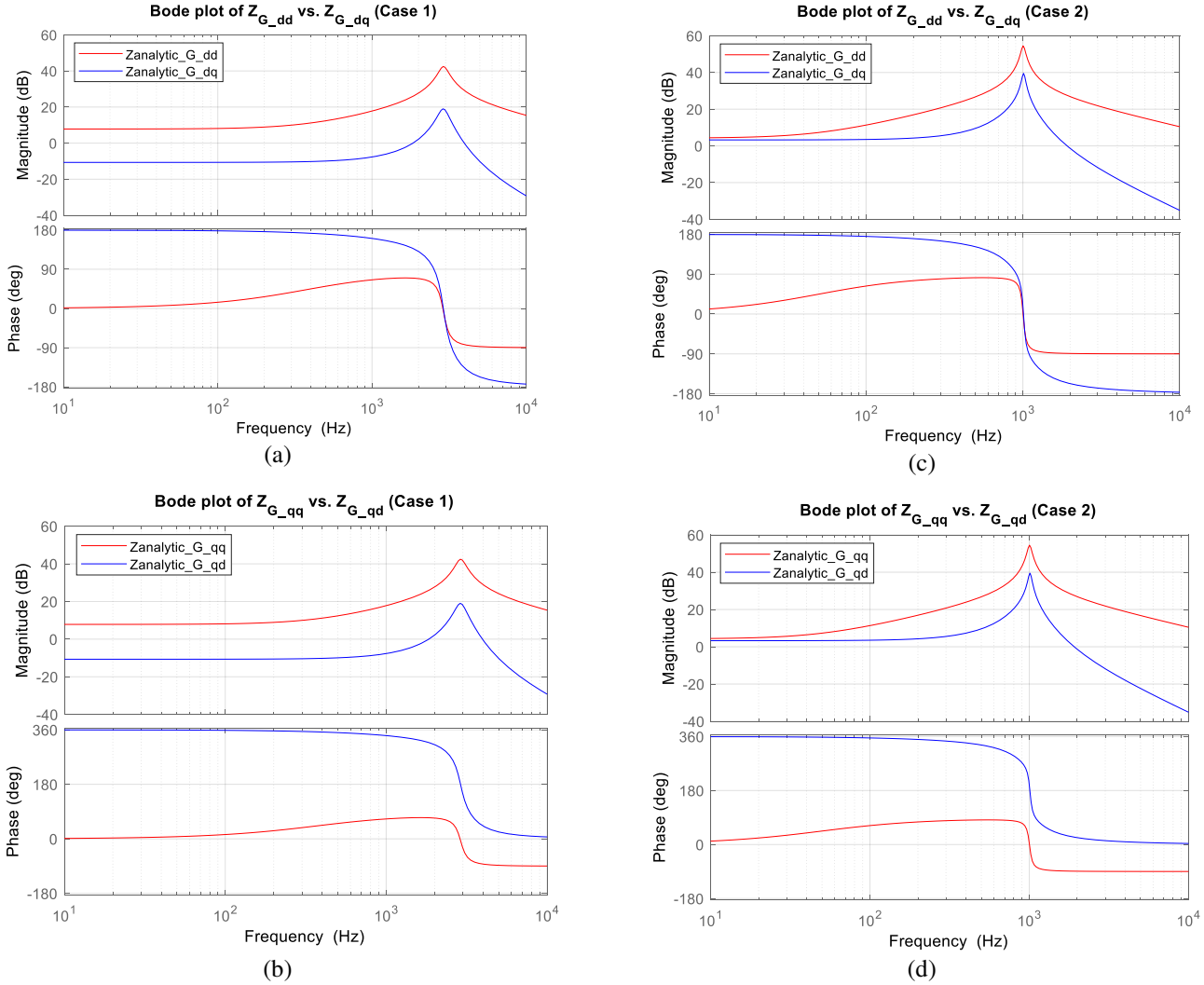

Fig. 7. Analytic grid impedance for Case 1 (a)-(b), and Case 2 (c)-(d).

IV. The Wideband System Identification Technique

In this section, the principle of operation of the WSI technique is presented. First, the technique on how to identify the grid impedance is given. Then, that one of the inverter output impedance is explained. Both the grid impedance and inverter output impedance are identified in *dq* domain. The main feature of the WSI technique is its natural characteristic to be integrated into the control of the inverter so that it can be used as an online monitor for grid stability applications as it will be shown in Section VI. The choice of the identification in *dq* domain comes as requirement from the inverter control which is implemented in such a domain as shown in Section III. This choice reduces the propagation of errors and limits the delays given by extra transformations if other modeling domains are selected.

A. Grid Impedance Identification in dq domain

This subsection presents the online WSI technique exploiting an existing grid-tied feedback-controlled inverter to identify the grid impedance in the *dq* domain. The WSI technique is based on the *perturb-and-observe* principle. The peculiarity of this technique is in how the perturbation is realized. Instead of performing a small-signal frequency sweep which requires long injection times, a short-time small-signal PRBS is used as test signal. PRBS is a digital approximation of white noise, therefore wideband in nature, and this allows creating a short-time wideband perturbation at the impedance measurement point.

Fig. 8 (a) shows the block diagram for the wide bandwidth identification of three-phase AC power grid impedance in *dq* domain. The inverter, in addition to performing its original power conversion function in either current or voltage mode, serves as power amplifier for the injected PRBS and as sensor of voltages and currents in *dq* domain. To identify the impedance of the three-phase system under test, i.e. the grid impedance in *dq* coordinates, the voltages and currents measurements in *dq* domain are processed in the integrated control platform to identify in real time the parametric impedance $Z_{G\_dq}(s)$. Notice that both the PRBS generator and processing are implemented in such an integrated control platform.

In practice (see Fig. 8 (b)), small-signal PRBS is added to the duty cycle and to both the current and voltage reference signals of the inverter controller. The reason for such a choice is linked to the frequency response of the closed-loop inverter. Fig. 9 shows a simplified small-signal block diagram of a converter employing an inner current loop and an optional outer voltage loop. The transfer function Z_{load} represents the impedance of the load subsystem, and *PRBS_1*, *PRBS_2*, and *PRBS_3* represent the disturbance injection at the duty cycle, current reference, and voltage reference, respectively.

The operation in current mode is analyzed first. By inspection of Fig. 9 with the switch connected to I_{d_ref}, the output voltage is given as follows.

$$v = G_{vd}\frac{\frac{1}{1+T_I}}{1+\frac{Z_{out}}{Z_{load}}}PRBS\_1 + \frac{G_{vd}}{G_{i_Ld}}\frac{\frac{T_I}{1+T_I}}{1+\frac{Z_{out}}{Z_{load}}}PRBS\_2 \qquad (21)$$

where G_{vd} is the control to output transfer function, G_{iLd} is the control to inductor current transfer function, Z_{out} is the output impedance, and T_I is the current control loop gain defined in Fig. 9.

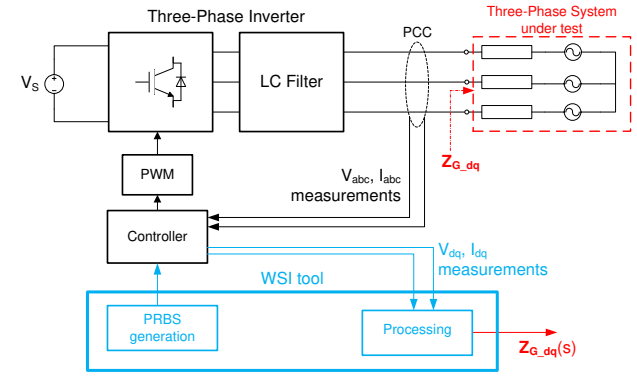

(a)

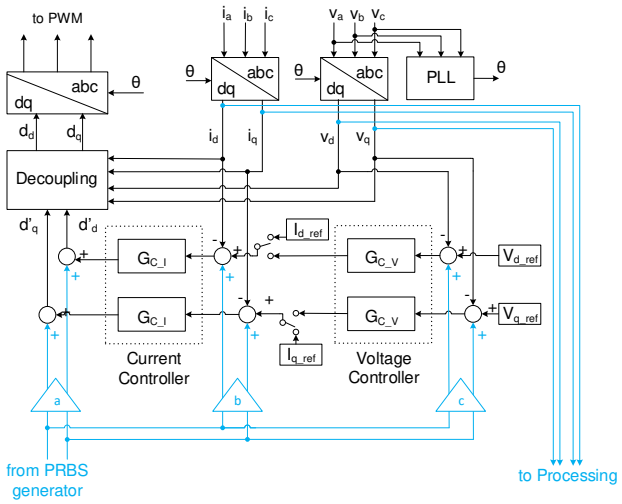

(b)

Fig. 8. Block diagram of the WSI technique to identify the grid impedance (a), and detailed inverter control implementation and its interface to the WSI tool (b).

Now, the operation in voltage mode is analyzed. By inspection of Fig. 9 with the switch connecting the outer voltage loop, the output voltage is given as follows.

$$\begin{aligned} v = {} & G_{vd}\frac{\frac{1}{1+T_I}}{1+\frac{Z_{out}}{Z_{load}}+T_V\frac{G_{vd}}{G_{i_Ld}G_{vc\_I}}\frac{T_I}{1+T_I}}PRBS\_1 \\ & + \frac{G_{vd}}{G_{i_Ld}}\frac{\frac{T_I}{1+T_I}}{1+\frac{Z_{out}}{Z_{load}}+T_V\frac{G_{vd}}{G_{i_Ld}G_{vc_I}}\frac{T_I}{1+T_I}}PRBS\_2 \\ & + T_V\frac{G_{vd}}{G_{i_Ld}G_{vc\_I}}\frac{\frac{T_I}{1+T_I}}{1+\frac{Z_{out}}{Z_{load}}+T_V\frac{G_{vd}}{G_{i_Ld}G_{vc\_I}}\frac{T_I}{1+T_I}}PRBS\_3 \end{aligned} \qquad (22)$$

where T_V is the voltage control loop gain defined in Fig. 9 and G_{vc_I} is the control current to output transfer function [37].

The controllers under consideration in this paper are PI controllers. If correctly designed, the current loop is very large in magnitude within the control bandwidth, while it is very small beyond the control bandwidth [37]. Therefore, the following quantities can be approximated as

$$\frac{T_I}{1+T_I} \approx \begin{cases} 1 & for\ \|T_I\| \gg 1 \\ T_I & for\ \|T_I\| \ll 1 \end{cases} \qquad (23)$$

$$\frac{1}{1+T_I} \approx \begin{cases} \frac{1}{T_I} & for \ \|T_I\| \gg 1 \\ 1 & for \ \|T_I\| \ll 1 \end{cases} \quad (24)$$

By using the results of Eqs. (23) and (24), the following statements are true:

- If only *PRBS_1* is applied, *v* has smaller amplitude than *PRBS_1* within the frequency range where T_I is very large, i.e. within the control bandwidth, while it has the same amplitude at larger frequencies.
- If *PRBS_2* (or *PRBS_3*) is applied, *v* has the same amplitude of the injected disturbance within the frequency range where T_I is very large, i.e. within the control bandwidth, while is reduced in amplitude at larger frequencies.

In other words, if PRBS is injected to the duty cycle only, PRBS, seen as a disturbance, is rejected within the bandwidth of the selected control loop (either current or voltage), while it is not rejected beyond the bandwidth of the selected control loop. On the other hand, if PRBS is injected to the current or voltage reference signals, it is not rejected within the bandwidth of the selected current or voltage control loop, respectively. Therefore, injecting PRBS to the duty cycle and to either the current or voltage reference signals ensures that PRBS is not rejected by the selected control action over a wide frequency range.

Notice from Fig. 8 (b) that the injected PRBS requires proper scaling to obtain the desired controlled perturbation amplitude at the impedance measurement point. This can be accomplished by properly choosing the scaling factors *a*, *b*, and *c* before being added to the duty cycle, current reference, and voltage reference, respectively. To maintain a small-signal perturbation at the impedance measurement point, e.g. between 5% and 10% of AC voltage and current steady state values, and considering that $PRBS\_1 = PRBS\_c \cdot a$ (likewise $PRBS\_2 = PRBS\_c \cdot b$ and $PRBS\_3 = PRBS\_c \cdot c$), where *PRBS_c* is that one coming from the integrated control platform, the scaling factors *a* and *b* (or *c*) can be calculated from (21) and (22) in the frequency range where PRBS is not rejected. Notice that because of (23) and (24), special care is required in the calculations of *a* and *b* (or *c*) in order to obtain a flat perturbation over the spectrum of interest.

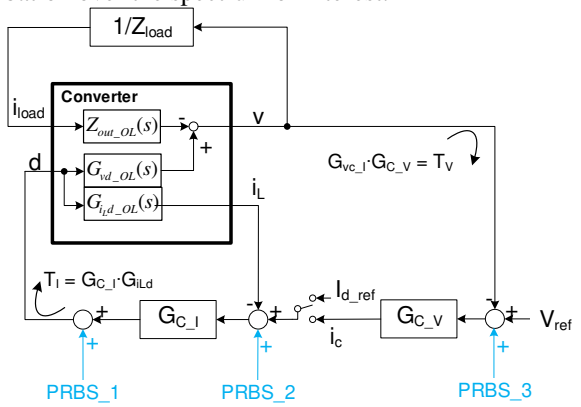

Fig. 9. Simplified small-signal block diagram representation of a converter with inner current loop and outer voltage loop as well as PRBS injection.

The impedances to be identified are the *dq* domain impedances of the Thévenin equivalent impedances of the balanced three-phase grid seen at the PCC, which is modeled as Y-connected configuration as depicted in Fig. 8 (a). In order to identify all the *dq* components of the grid impedance, PRBS is first injected on the *d*-component only and then on the *q*-component only according to the injection scheme shown in Fig. 8 (b). Assuming that the system frequency is constant, the four impedances are sequencially constructed as follows:

$$Z_{G\_dd} = v_d/i_d \ and \ Z_{G\_dq} = v_d/i_q \quad (25)$$

$$Z_{G\_qq} = v_q/i_q \ and \ Z_{G\_qd} = v_q/i_d \quad (26)$$

Notice that orthogonal PRBSs can be generated which allow simultaneously identifying *d* and *q* components of the impedance of the three-phase system under test [21].

B. Inverter Output Impedance Identification in dq domain

This subsection shows how the same WSI tool can be used to online identify the output impedance of the inverter with few modifications and without the addition of any extra power hardware. Fig. 10 shows how the WSI tool is connected to the grid-tied inverter system. In this case, PRBS is injected into the three-phase grid voltage sources of the load subsystem. Since PRBS is generated in the *dq* domain, it has to be transformed in the *abc* reference frame to be injected into these grid voltage sources. This is accomplished by using a dedicate Phase Locked Loop (PLL). This representation is surely fictitious but clearly mimics, in a lumped manner, a more complex system, e.g. that one of Fig. 1 (b), where other grid-tied inverters are also able to perform the injection task (but also the identification task) on the top of their power conversion function. To identify the impedance of the three-phase system under test, i.e. the inverter output impedance, the voltages and currents measurements in *dq* domain are processed in the integrated control platform to identify in real time the parametric impedance $Z_{S\_dq}(s)$.

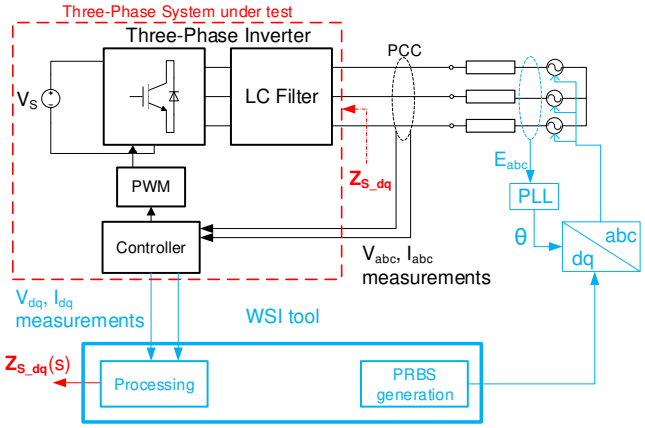

Fig. 10. Block diagram of the WSI technique to identify the inverter output impedance.

According to the implementation described above, to identify all the *dq* components of the inverter output impedance, PRBS is first generated on the *d*-component only and then on the *q*-component only. Then, thanks to the use of the dedicated PLL, PRBS is synchronously added to the three-phase voltage sources. Assuming that the system frequency is constant, the four impedances are constructed as follows:

$$Z_{S\_dd} = -v_d/i_d \ and \ Z_{S\_dq} = -v_d/i_q \quad (27)$$

$$Z_{G\_qq} = -v_q/i_q \text{ and } Z_{S\_qd} = -v_q/i_d \quad (28)$$

Notice that the positive direction of the current is from the source to the load subsystem.

V. The Hardware-In-the-Loop Real-Time Setup

In this section, the HIL real-time setup for online parametric three-phase impedance identification is presented. The description of the full implementation of the WSI technique in the integrated control platform is provided.

A. The HIL Setup

The HIL setup, shown in Fig. 11, consists of a real-time simulator, i.e. eMEGAsim from OPAL-RT Technologies [34], where a digitally-controlled switching-type inverter connected to a lumped grid model is implemented. OPAL-RT is connected to a RT host PC with the NI LabVIEW RT OS and a NI PCIe-7841R RIO [35], where the PRBS generator, data acquisition (DAQ) and calculation of grid impedance are implemented.

The eMEGAsim simulator is equipped with an OP5600 hardware platform. The hardware configuration of the simulator includes two six-core Intel CPUs and a Xilinx Virtex-6 Field Programmable Gate Array (FPGA). Moreover, the simulator is equipped with 16 16-bit AOs and 16 16-bit AIs, and 32 DOs and 32 DIs. The eMEGAsim is based on RT-LAB, an open real-time simulation environment, which is fully integrated with Simulink/Simscape by Mathworks. The RT-LAB for OPAL-RT systems link Simulink models to both the CPUs and the FPGA. RT-LAB generates and compiles real-time code that runs on the OP5600 hardware. The RT-LAB augments the standard Simulink library with a custom blockset that gives the user access to I/O ports, PWM, power electronic, and various other event handling and timing systems on the OP5600 hardware.

As previously stated, the PRBS generator, data acquisition and calculation of grid impedance are implemented in an RT host PC through LabVIEW. This choice is justified by the fact that the implementation of the impedance identification technique requires a large amount of memory and high-performance ADCs and DACs. For this purpose, the chosen platform is equipped with a Direct Memory Access (DMA) FIFO channel to buffer the data, and 8 16-bit AIs and 8 16-bit AOs. Moreover, the NI RIO device contains a Virtex-5 FPGA programmable with the LabVIEW FPGA Module that can be used for this implementation due to its inherent multi-threaded architecture, and its ability to interface to ADC/DAC and memory.

The chosen HIL setup emphasizes the fact that the identification tool can be simply integrated into an existing inverter controller as long as the tool has access to the inverter measurements in *dq* domain and has the ability to add the PRBS injection over the inverter control loop as explained in Section IV. Notice that implementation in an embedded controller is feasible if the chosen platform that hosts the WSI tool is provided with enough dedicated memory.

B. The Simulated System

The upper part of Fig. 11 shows the block diagram of the system, running in the real-time digital simulator, to identify the grid impedance and the inverter output impedance according to the PRBS injection and identification mechanisms explained in Sections IV.A and IV.B. The grid-connected system consists of a feedback-controlled three-leg bridge inverter and grid impedance, whose full description was given in Section III. To implement the bridge switches with no dead-time, a special RT block from OPAL-RT libraries is used as it will be explained in Section V.D. The PRBS signal is sequentially injected upon the *d*- and *q*- components of the control loop of the inverter as explained in Section III. The *dq* components of currents and voltages at the PCC are used to construct the *dq* wideband grid impedances according to the procedure explained in Section III. The simulation model implemented in OPAL-RT runs in the CPU, while the D/A and A/D conversions are implemented in the FPGA. The simulation time step is 25 µs.

C. The Implementation of the WSI Technique

The implementation of the WSI algorithm is divided in multiple stages as depicted at the bottom part of Fig. 11. The first stage consists of the PRBS generation and simultaneous data acquisition (DAQ). The following stages realize the data processing and identification of the parametric impedance.

1) PRBS Generation

To generate the PRBS, a 15-bit linear feedback shift-register (LFSR) is implemented in FPGA. The XOR-ed value of bit 14 and bit 15 are fed back to the beginning of the register, as depicted in Fig. 12. The last value of the register is shifted to achieve a white-noise approximation with zero mean [14]. Then, PRBS is routed to OPAL-RT using two channels (one for *d*-component and one for *q*-component) of the analog output port at a rate that can be chosen (25 µs for this HIL setup). The PRBS signal is then properly scaled and added to the duty cycles and the control reference signals of the inverter, as shown in Fig. 8 (b). The amplitude of PRBS can be selected; it is recommended to produce a perturbation between 5% and 10% of the steady-state operating point as explained in Section IV.

2) Data Acquisition (DAQ)

While PRBS is being generated and injected, taking advantage of parallel computation of the FPGA, the current and voltage signals in *dq* coordinates coming from OPAL-RT are sampled using four AIs with a sampling rate that can be chosen (25 µs for this HIL setup). The acquired time window during which PRBS is injected and voltages and currents are measured can also be chosen (200 ms for the results presented in this paper). The voltage and current samples are directly written in the memory of the host PC through a DMA channel. This "First-In First-Out" (FIFO) architecture allows buffering the sampled values and processing them as a batch after the DAQ is completed. The PRBS signal is only injected during the DAQ phase and turned off immediately after the complete time window is acquired.

1) Fast Fourier Transform (FFT)

The proper voltage and current in the *dq* domain are selected to build the identified impedance according to (25)-(26) for the grid impedance or to (27)-(28) for the inverter output impedance. Voltage and current spectra are calculated by performing an FFT algorithm. A Hanning windowing is applied.

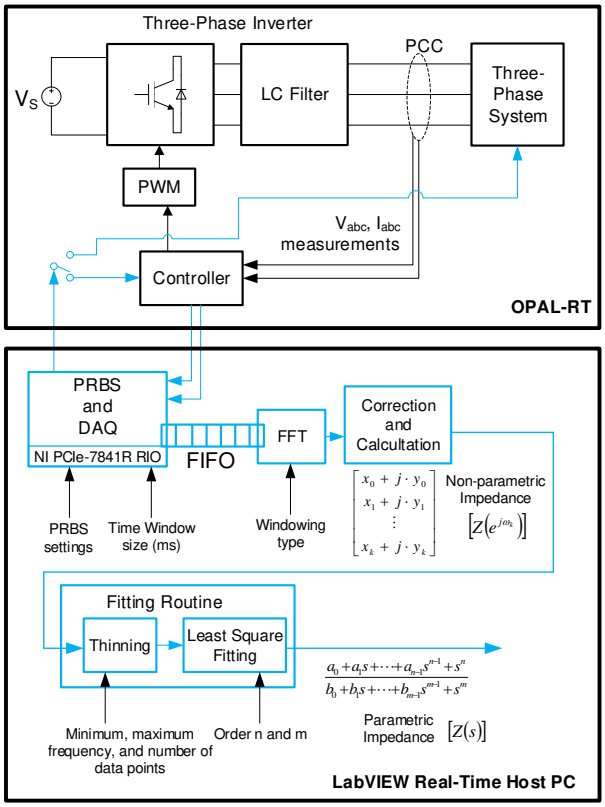

Fig.11. Block diagram of the HIL setup showing both the real-time simulation system and the WSI technique implementation.Correction and Calculation

A correction routine is performed to cancel the existing harmonics besides the AC system fundamental frequency because this latter is already canceled out by the synchronous *abc*-to-*qd* transformation. The cancellation of harmonics is performed by subtracting the voltage and current spectra obtained under PRBS perturbation from those obtained without any injection [25]-[28]. Then, dividing voltage and current spectra yields the non-parametric grid impedance as follows

$$Z[e^{j\omega_n}] = \frac{FFT\{v[n]\}}{FFT\{i[n]\}} \tag{29}$$

where $v[n]$ and $i[n]$ are the voltage and current samples. The non-parametric impedance consisting of N complex data points:

$$N = t_{window} \cdot f_{sampling} \tag{30}$$

where t_{window} is the observation window during which PRBS is injected and voltage and current are measured and $f_{sampling}$ is the sampling frequency of $v[n]$ and $i[n]$.

2) Fitting Routine

The fitting routing consists of a real time algorithm able to return the parametric impedance from the non-parametric data set. The complete fitting routine is implemented using a "Mathscript Node", which allows including MATLAB code to be executed on the LabVIEW Real-Time Host PC. This yields access to a large number of powerful functions for data manipulation and processing. The fitting consists of two steps: data thinning and least square fitting. The thinning enforces equal weighting over the full frequency window of the non-parametric data. The thinning technique is used to obtain a logarithmically spaced subset of the data points. In order to do so, the lower and upper frequency boundaries for the data thinning routine have to be specified. All data points outside this window are disregarded for further processing. The least square fitting routine matches the thinned data to a polynomial function and it is an algorithm based on Levy [44]. The order of numerator n and denominator m must be selected. If they are not known a priori, the order can be tentatively estimated by increasing n and m until the fitting result matches the non-parametric impedance. The result of the fitting routine is the parametric impedance, given by the coefficients of a polynomial function, whose generic representation is also given in Fig. 11.

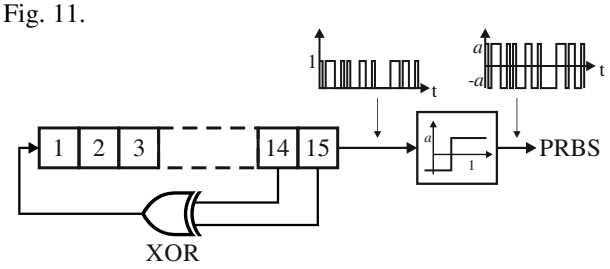

Fig. 12. Block diagram of LFSR for PRBS generation.

D. Performance of the WSI Technique and Overcoming Practical Challenges

The real time performance of the WSI technique is given by the execution time of all the routines described in the previous subsection starting from when the PRBS injection is activated and ending when the parametric impedance result is available. The execution time of the implemented WSI technique consists of the chosen time window and the impedance calculation time. The impedance calculation time comprises the execution time of the FFT algorithm, which is of complexity $O(N \cdot log(N))$, and the fitting routine, which depends on exit conditions of the least-square fitting algorithm [44]. Both the algorithms are estimated to have an execution time of 20 ms. Therefore, to measure a single component of the impedance of the system under test, the implemented WSI technique takes about $t_{window} + 20\ ms$.

A major challenge in impedance identification consists of maintaining the small-signal condition and, at the same time, guaranteeing a measurable perturbation within the frequency range of interest. In theory, the maximum identifiable frequency is defined by the Nyquist frequency, i.e. half the switching frequency of the inverter [14]-[20]. The lower frequency boundary, instead, is equal to the inverse of the measured time window t_{window} during which the PRBS is injected. In practice, the upper boundary depends on the amplitude of the injected PRBS signal. In fact, the LC filter of the inverter attenuates the high frequency perturbation, eventually leading to a signal level that is comparable with the noise floor ($< -60\ dB$) and therefore too small to be identified. As a consequence, the attenuation at high frequencies introduced by the LC filter dictates the minimum amplitude of the injected PRBS signal. Therefore, to obtain a good identification as close as possible up to the Nyquist frequency, despite the attenuation of the LC filter, and maintaining at the same time the small-signal condition, a good choice is to perturb voltage and current with magnitude between 5% and 10% of their steady-state value. As an alternative solution, a

different perturbation signal may be used; an alternative to white noise is blue noise which increases the high-frequency content of the PRBS without affecting the low-frequency content. The implementation of a blue noise filter for identification purposes in described in [16]-[17]. As another efficient alternative, discrete-interval binary sequence can be used [48]. This latter technique allows specifying the harmonics so that the injection spectral energy can be maximized without the need of increasing the pertubation signal amplitude.

The choice of the time window is another practical challenge worthy of discussion. As the time window is directly linked to the number N of complex data points of the non-parametric impedance according to (30), for a fixed sampling rate, a long enough time window should be selected in order to have enough data points to capture eventual sharp features of the identified impedance, such as lightly damped resonances. On the other hand, the time window should be chosen short enough to avoid increasing impedance calculation times. Moreover, how short the time window should be chosen is in relation to the characteristics of the DUT. For the Power-Electronics-based AC Power System of Fig. 1 (b), it is important to set the time window short enough in order to catch with fast changing impedances for example due to load steps or system reconfiguration.

Cancellation of existing harmonics is another challenge that requires special attention. The grid-connected power electronic system is time-variant and the correction procedure as described earlier is affected by this characteristic. The FFT assumes infinite periodicity of the signal to be transformed. However, such an assumption is not practical because all the signal acquisitions are limited in time. During the acquisition, the FFT returns additional spurious frequency components around the existing harmonic content because of the discontinuities at the edges of the time window when the number of the acquired periods is not an integer. This well-known problem is called spectral leakage [38] and it is the main reason for the non-perfect harmonic cancellation. In order to minimize the effect of spectral leakage, two recommendations are made: 1) creation of Hanning window of the same length as the acquired signal, and 2) ensuring periodicity of the injection in synchronism with the acquisition over an integer number of fundamental frequency cycles (integer multiples of 20 ms for 50 Hz or 16.67 ms for 60 Hz).

Another practical aspect is the resolution of the D/A and A/D converters of both the real-time digital simulator and the NI RIO device. Low resolutions increase the minimum viable amplitude of the perturbation. Fortunately, both OPAL-RT and NI PCIe-7841R RIO are equipped with 16-bit D/A and A/D converters which give a resolution of 9.49 mV on a grid voltage measurement of 220 Vrms and a resolution of 0.31 mV on the injected PRBS of ±10 V. This setup enables accurate measurement even in the presence of small injected perturbations.

As far as the implemented real-time simulation in OPAL-RT, a proper choice of the simulation time step is critical. Such a choice allows obtaining not only reliable simulation results but also an accurate identification, especially at high frequencies. The ratio of simulated inverter switching period and simulation time step gives the number of duty cycle values that are possible in the simulation environment, which determines the effective PWM resolution in the simulation. For the case presented in this paper, the switching frequency is 20 kHz (Ts = 50 µs) and the fixed simulation time step is 25 µs. As a result, in the simulation only 2 possible values of duty cycle would be possible. To overcome this problem of poor duty cycle resolution, the PWM and the Time-Stamped Bridge modules, available in the OPAL-RT's RTeDriveTM and RT-EventsTM libraries, replace the counterpart PWM and Universal Bridge blocks available in SimPower Systems library. These special Simulink models can run on the CPU real-time target [39] and are supported by the solver eDRIVEsimTM, which is able to decouple the switching period from the simulation time step. This allows improving the time resolution of a switch-mode model for a given switching frequency and a fixed simulation time step.

VI. Results Of The Online Impedance Identification and Stability Analysis

In this section, both time and frequency domain results of the HIL setup are presented and discussed. These include the results of the online parametric identification of all the *dq* components of the interface impedances of the grid-tied current-controlled inverter system compared to the analytic impedances derived in Section III. The identified parametric impedances are used in the system stability analysis according to the generalized Nyquist stability criterion applied to the minor loop (13), i.e. that one when the source is current driven.

Fig. 13 shows a screenshot of the GUI used to set the settings of the WSI tool implemented in LabVIEW and for online result visualization. The GUI displays the following plots: at the top from left to right, acquired voltage and current measurements during the selected time window, voltage and current spectra after the FFT to the acquired voltage and current, and Bode plot of the identified non-parametric impedance as result of (20); at the bottom from center to left, the Bode plot of the thinned non-parametric impedance vs. the analytic impedance, and the Bode plot of the fitted parametric impedance vs. the analytic impedance. PRBS injection and DAQ settings are on the left hand side of the GUI. The user can choose the perturbation amplitude and rate as well as the channel of injection (three channels are available, but channel 1 is mapped to the *d*-component and channel 2 to the *q*-component). The sampling rate of voltage and current measurements can also be chosen as well as the time window during which PRBS in injected and signals are sampled. To construct the impedance of interest, proper voltage and current measurements have to be selected; for the screenshot of Fig. 13, the ratio V_1/I_1 returns the impedance Z_{dd}. The fitting settings are also available; the user can choose the number of thinned data points as well as the minimum and maximum frequencies that will be processed by the least square fitting routine. This latter requires the user to specify the orders of the numerator and denominator. The result of the fitting is the parametric fitted transfer function in the following form:

$$Z_{parametric}(\mathrm{s}) = \frac{a_0 + a_1 s + \cdots + a_{n-1} s^{n-1} + a_n s^n}{b_0 + b_1 s + \cdots + b_{m-1} s^{m-1} + b_m s^m} \qquad (31)$$

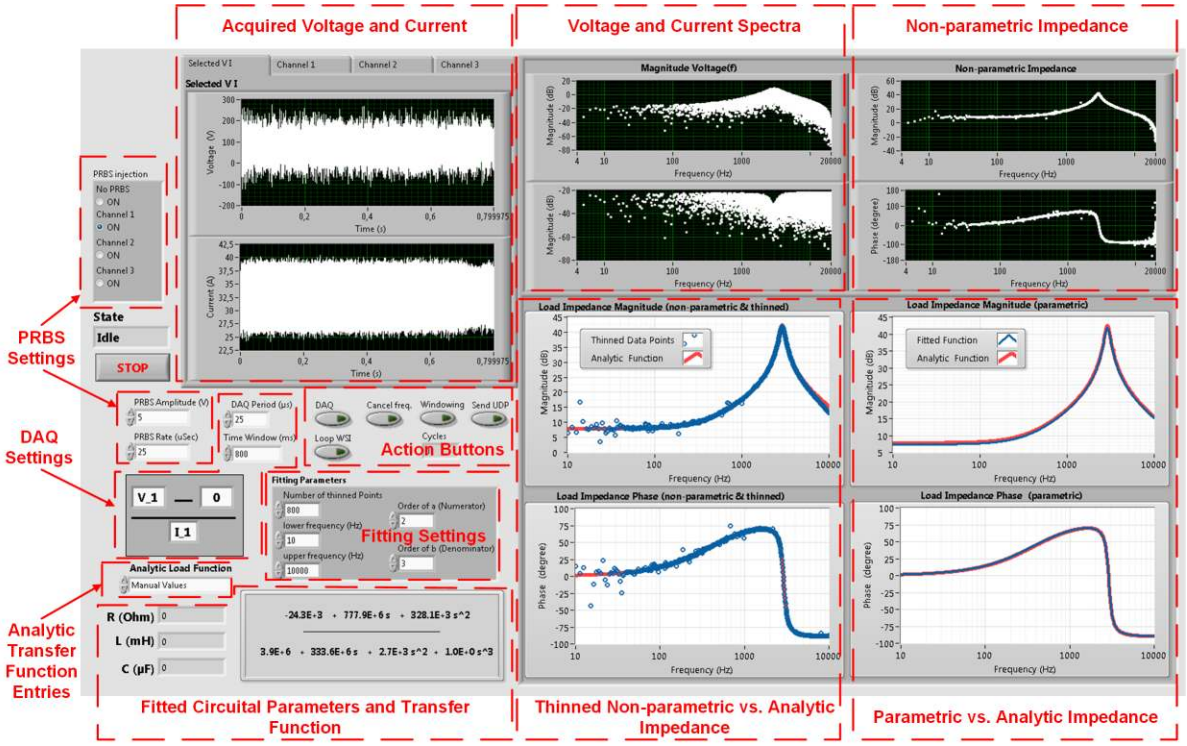

Fig. 13. Screenshot of the GUI of the WSI tool implemented in LabVIEW.

Alternatively, the circuital parameters can be extracted from the fitted parametric impedance if the topology of the system under test is known. Both the fitted transfer function in the form of (31) and the identified circuital parameters are shown at the bottom left corner of screenshot of the GUI and are updated in real time (every $t_{window} + 20\ ms$ as explained earlier). Some action buttons are displayed in the middle of the GUI. It is possible to perform the online parametric identification in single shot mode or looping mode (i.e. continuously injecting PRBS and identifying the impedance), to activate the cancellation mechanism of the existing frequencies as well as to activate the windowing to the FFT algorithm. Moreover, it is possible to send, via User Datagram Protocol (UDP), the coefficients of the fitted parametric impedance, i.e. the vectors $[a_0\ a_1 \cdots a_{n-1}\ a_n]$ and $[b_0\ b_1 \cdots b_{m-1}\ b_m]$, to a receiver PC to perform remote online stability analysis. The coefficients are transmitted as single-precision floating-point values consisting of 4 Bytes each.

A. *Online Parametric Identification of the Grid Impedance*

Initially the system is in steady-state without PRBS injection. Then, the identification procedure is initiated by injection of 10% 15-bit white noise PRBS over the *d*-channel first for a time window of *200 ms* and then over the *q*-channel for the same amount of time. Fig. 14 shows a time-domain capture of the inverter's voltage and current at the PCC during PRBS injection and without it. It can be seen that injected perturbation does not introduce an excessive amount of noise to the system.

Non-parametric grid impedances are identified by using (29) to (25) and (26). Then, the thinning technique is used to obtain a logarithmically spaced subset of 800 data points in the frequency range of *10Hz-10kHz*, and the least square fitting routine returns the parametric impedance. For the sake of validation of the accurateness of the identification technique with the present HIL setup, the online identified non-parametric and parametric grid impedances are compared in real time to the counterpart analytic model and plotted in the GUI as shown at the right bottom of the screenshot of Fig. 13. For a better visualization, the captures of the Bode plots from the GUI are shown in Figs. 15-16 for the grid impedance labeled as "Case 1" and "Case 2" (refer to Section III-B). Fig. 15 shows the Bode plot of the thinned non-parametric impedance vs. the analytic impedance, while Fig. 16 plots the parametric impedance vs. the analytic impedance. Only *dd* and *qq* components are parametrized (fitted transfer functions are in Appendix) because they are the components needed for the stability analysis according to (13). In all cases, very good matching is evident.

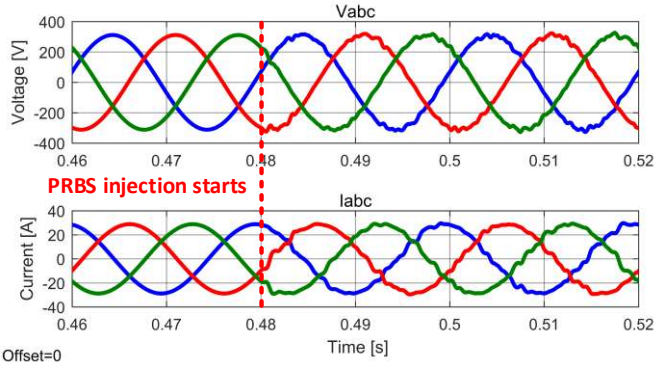

Fig. 14. Three-phase voltage current at the PCC during PRBS injection compared to their steady-state trend.

B. *Online Parametric Identification of the Inverter Output Impedance*

The identification of the inverter output impedance is more challenging than that one of the grid impedance due, on the one

hand, to the switching nature of the inverter, and, on the other hand, to the rejection effect of the current control. Looking at Fig. 10, PRBS is seen by the inverter as a load current disturbance. Similarly as done in Section IV-A, it can be demonstrated that PRBS is rejected within the current control bandwidth, while it is not at higher frequencies. As a result, the non-parametric identification of the inverter output impedance suffers from poor accuracy at low frequencies when the current spectrum hits the noise floor. To partially cope with such a difficulty, the lower frequency limit for the fitting routine was set to *30 Hz*. The same time window of 200 µs and 800 number of thinned points are used.

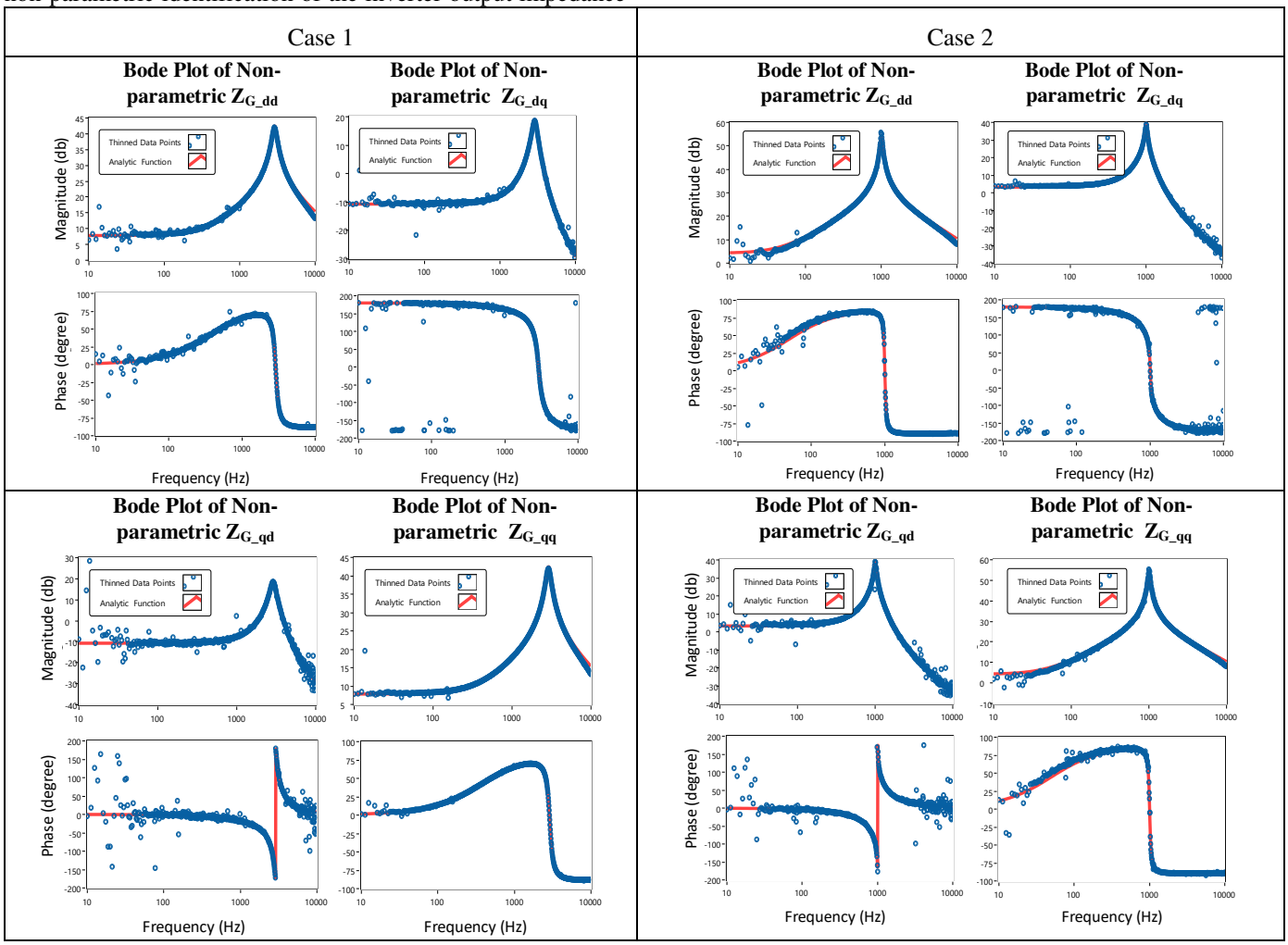

Fig. 15. Bode plot of the identified thinned non-parametric impedance vs. the analytic impedance for the grid impedance – Case 1 and Case 2.

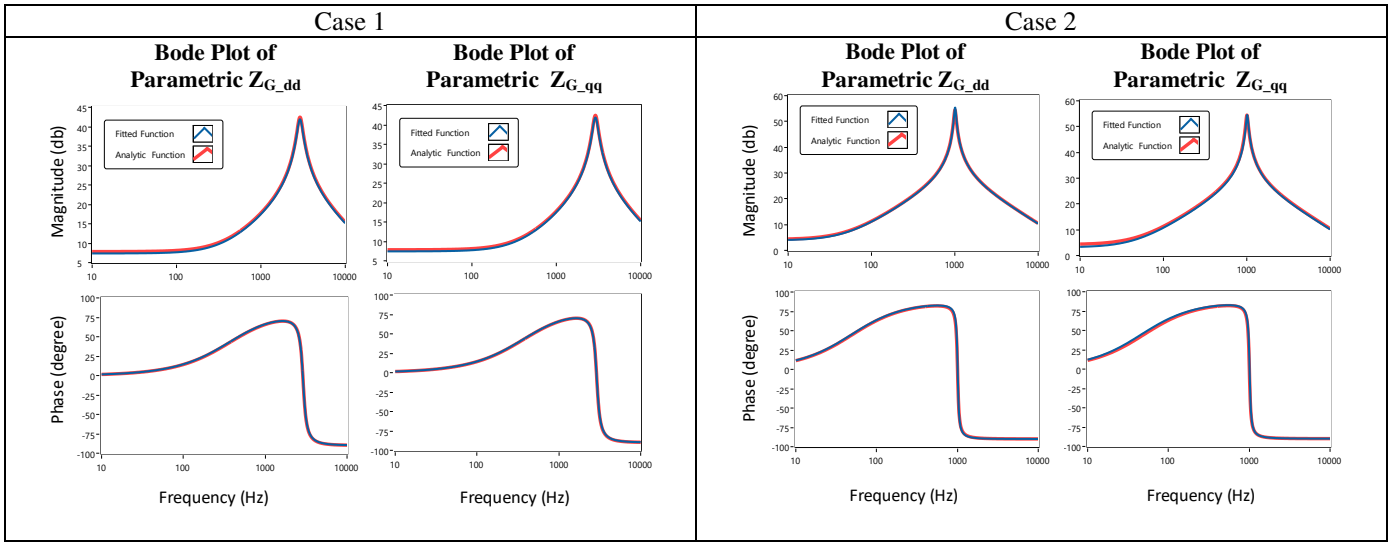

Fig. 16. Bode plot of the identified parametric impedance vs. the analytic impedance (only *dd* and *qq* components) for the grid impedance – Case 1 and Case 2.

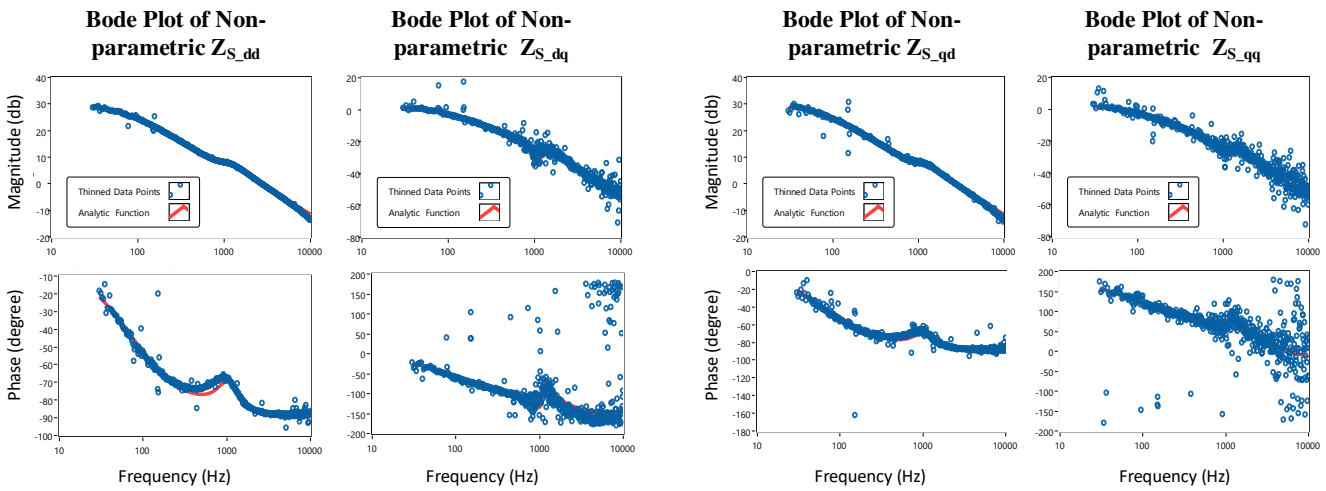

Fig. 17. Bode plot of the thinned non-parametric impedance vs. the analytic impedance for the inverter output impedance.

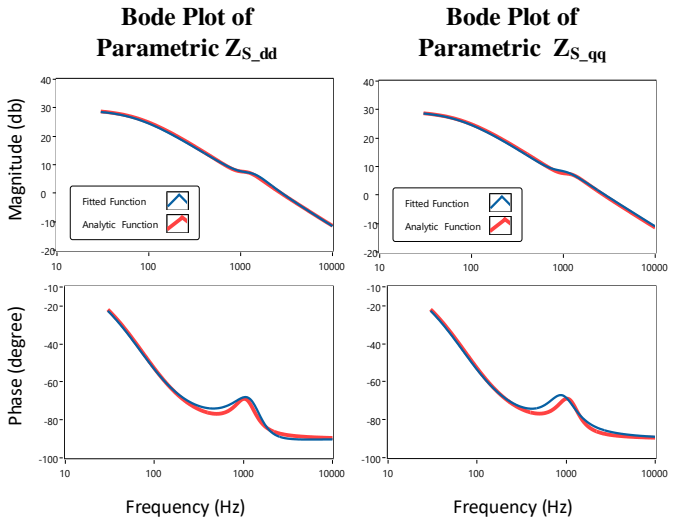

Fig. 18. Bode plot of the parametric impedance vs. the analytic impedance (only *dd* and *qq* components) for the inverter output impedance.

Non-parametric grid impedances are identified by using (29) to (27) and (28). Figs. 17-18 show the captures of the Bode plots of the inverter output impedance from the GUI of the WSI tool in LabVIEW. Fig. 17 shows the Bode plot of the thinned non-parametric impedance vs. the analytic impedance, while Fig. 18 plots the parametric impedance vs. the analytic impedance. Again, only *dd* and *qq* components are parametrized (fitted transfer functions are in Appendix) because they are the components needed for the stability analysis according to (13). In all cases, again, very good matching is evident.

C. Stability Analysis

The current-controlled inverter system is tested with two grid impedances labeled as Case 1 and Case 2, whose circuital parameters are given in Table II. To perform the stability analysis of the inverter system, the fitted coefficients $[a_0\ a_1 \cdots a_{n-1}\ a_n]$ and $[b_0\ b_1 \cdots b_{m-1}\ b_m]$ of the identified parametric impedances $Z_{param\_S\_dd}(s)$, $Z_{param\_S\_qq}(s)$, $Z_{param\_G\_dd}(s)$, and $Z_{param\_G\_qq}(s)$ are transmitted via a UDP to a receiver PC. A MATLAB script in this PC loads the coefficients, constructs the impedances according to (31), and, in line with (13), plots the Nyquist diagram of the following minor loop gains:

$$T_{MLG\_dd} = \frac{Z_{paramc\_G\_dd}(s)}{Z_{param\_S\_dd}(s)} \tag{32}$$

$$T_{MLG\_qq} = \frac{Z_{param\_G\_qq}(s)}{Z_{param\_S\_qq}(s)} \tag{33}$$

It was demonstrated in Section III that both the inverter output impedance and grid impedance are diagonally dominant. This was also confirmed by the online measurements. Therefore, it makes sense to perform the stability analysis on the minor loop gains (32) and (33). Fig. 19 shows the Nyquist diagram of the minor loop gains (32) and (33) that use the transmitted fitted parametric coefficients of the impedances identified by the online WSI tool. The Nyquist contour for both Case 1 and Case 2 do not encircle the $(-1, j0)$ point, thus predicting a stable inverter system for both situations. However, the phase margin for the inverter system with the grid impedance labeled as Case 1 is larger than for Case 2. This predicts that the inverter system with grid impedance labeled as

Case 1 is more robustly stable than Case 2. Notice that only $T_{MLG\_dd}(s)$ could have been used for assessing the system stability because $Z_{param\_S\_dd}(s) = Z_{param\_S\_qq}(s)$ due to the fact that in this paper the dynamics of the PLL have been neglected. If the dynamics of the PLL are included the system becomes unsymmetric and $Z_{param\_S\_dd}(s) \neq Z_{param\_S\_qq}(s)$ [45]. Therefore, both (32) and (33) needed to be used to assess the system stability [8]-[10].

Fig. 20 depicts the transient current response of the inverter system in correspondence of a current step from I_{d_ref} (defined in Fig. 4) to 50 A. When the inverter is connected to the grid impedance labeled as Case 2, the *dq*-components of the current result in a more oscillatory trend with respect to those of Case 1, especially the *q*-component. The time domain results are perfectly in line with the frequency-domain stability prediction.

VII. Conclusions And Future Work

This paper presents the implementation of a noninvasive online Wideband Systems Identification (WSI) technique in a RT LabVIEW target to online identify three-phase parametric interface impedances in *dq* domain of a grid-tied feedback-controlled inverter system. The accuracy and performance of the implemented WSI tool is evaluated through a HIL setup, comprising a grid-connected switch-mode feedback-controlled inverter running in real-time in OPAL-RT. The chosen HIL setup emphasizes the fact that the WSI identification tool can be simply integrated into an existing inverter controller as long as the tool has access to the inverter voltage and current measurements in *dq* domain, and has the possibility to add the PRBS injection over the inverter control loop. The full description of the HIL setup and all the routines of the implemented WSI tool are provided. Technical challenges are also discussed and implemented solutions are presented. Frequency domain results reveal high accuracy of the implemented WSI tool in the *dq* domain parametric identification of balanced three-phase interface impedances. The online parametric identified interfaces are then used to assess the stability of the grid-tied inverter system by applying the generalized Nyquist stability criterion to the minor loop gain of the inverter/grid interface. Results in the frequency domain predict the system stability in accordance with the time domain results.

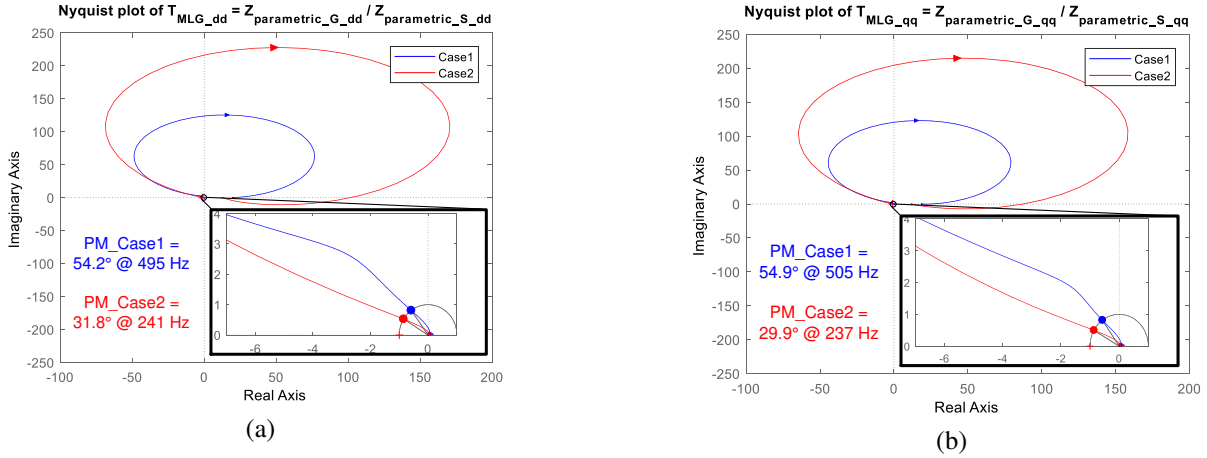

Fig. 19. Nyquist plot of $T_{MLG\_dd}(s)$ (a) and $T_{MLG\_qq}(s)$ (b) then the grid impedance is as Case 1 and Case 2.

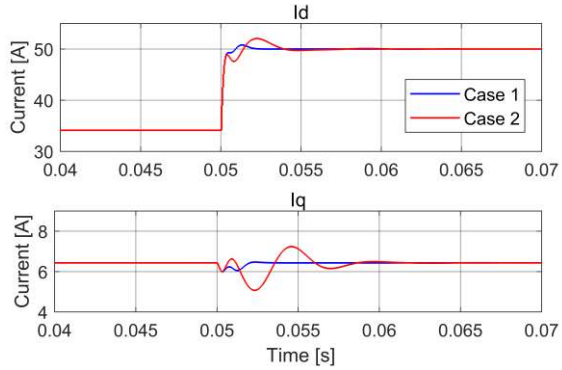

Fig. 20. Current transients in corrispondence of a current step on the *d* component when the grid impedance is as Case 1 and Case 2.

Notice that in the paper the identification of impedances and stability analysis were performed in *dq* domain, thus resulting with some extra analysis to assess whether the off-diagonal elements of the impedance matrices can be effectively neglected. Such a difficulty is completely avoided if the phase sequence domain is used because this modeling method "yields decoupled positive- and negative-sequence converter impedances, when phase- or *dq*-domain current control systems are implemented" [47]. This feature enables several practical advantages of the phase sequence domain over the *dq* domain [46]: 1) SISO stability analysis for balanced three-phase systems, 2) both balanced and unbalanced systems can be handled, and 3) the impedances depend only on the converter dynamics and not on the system frequency. Therefore, future work will need to look into the phase sequence domain for the impedance identification and make a comparative study to the identification in *dq* domain.

Moreover, as underling assumptions, the paper has dealt with ideal PLL and constant system frequency. In a real system where the PLL has its own dynamics and the system frequency may vary, injecting a pure *d*-component and pure *q*-component PRBS is challenging, and this may corrupt the impedance identification accuracy. Future work will look into a more realistic situation when a real PLL and a system frequency control are deployed. Practical requirements and conditions for the frequency control and the PLL to assure proper PRBS injection and accurate impedance measurements will need to be

found.

Future work will also need to look into the dynamic effect of a real PLL on the identified impedances. In such a case, it will be shown that the WSI tool will be able to measure different parametric impedance *dd* and *qq* components (phase of *qq* components starts at −180° at low frequency), but the *dq* and *qd* components are the same in magnitude (except 180° phase shift). In practice, from the online parametric impedance identification, the negative incremental resistance behaviors of output and input impedances of grid-connected feedback-controlled inverters and active rectifiers will be captured. From the stability analysis standpoint, therefore, the PLL will be identified as the main responsible for potential stability problems in LV Power-Electronics-based AC Power Systems. This result will be compared to those of [8]-[10], where nonparametric impedances were used for stability analysis. Also, the practical advantages of parametric identification over nonparametric identification will be sistematically presented in a special remote online stability analysis setup. By referring to Fig. 21, a real-time application in a secondary substation will not only be coordinating the injection of PRBS at the converters connected to the several PCCs, but also acquiring from a communication link the coefficients of the parametric impedance identifications (red arrows) and build the corrispondent minor loop gains out of which stability margins can be calculated in near real-time as well. If stability margins violate certain conditions, then corrective stabilizing actions can be taken (blue arrows).

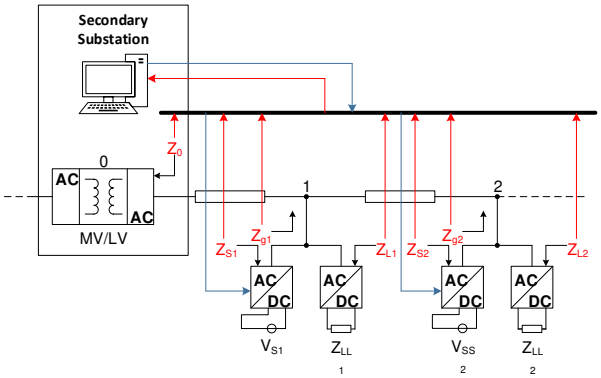

Fig. 21. Power-Electronics-based LV Feeder equipped with a communication link to perform stability analysis at substation level.

Finally, another piece of future work will focus on the derivation of a modeling framework in *dq* domain of grid-connected power electronic converters with real PLLs. This modeling framework will not only capture the dynamics of PLLs, but going beyond what already published in [8], it will include the requirement of taking into account the topology of the power system of Fig. 21 so that of being easily applicable to well-known impedance-based stability criteria. In practice, the modeling framework will end up with a matrix of a kind of mixed nodal admittance matrix which includes the inteface impedances at the various PCC of the system.

APPENDIX

Analytic expressions for the inverter output impedances:

Inverter in Current Mode	Inverter in Voltage Mode
$Z_{analytic\_S\_dd} = Z_{analytic\_S\_qq} =$ (1.67e04*s^3 + 1.161e08*s^2 + 8.865e11*s + 1.492e15)/(s^4 + 7483*s^3 + 6.644e07*s^2 + 1.387e11*s + 5.086e13)	$Z_{analytic\_S\_dd} = Z_{analytic\_S\_qq} =$ (1.669e04*s^3 + 7.563e07*s^2 + 6.889e11*s + 6.342e11)/(s^4 + 5115*s^3 + 5.449e07*s^2 + 4.46e10*s + 4.581e13)
$Z_{analytic\_S\_dq} = -Z_{analytic\_S\_qd} =$ (47.68*s^3 + 6.261e06*s^2 + 7.7e09*s + 2.968e14)/(s^4 + 1.259e04*s^3 + 8.89e07*s^2 + 5.447e11*s + 2.317e14)	$Z_{analytic\_S\_dq} = -Z_{analytic\_S\_qd} =$ (5.85e06*s^4 + 8.486e09*s^3 + 2.582e14*s^2 - 4.978e15*s + 4.037e17)/(s^6 + 1.171e04*s^5 + 8.768e07*s^4 + 5.462e11*s^3 + 5.017e14*s^2 + 4.747e17*s + 4.971e19)

Analytic expressions for the grid impedance:

Grid Impedance – Case 1	Grid Impedance – Case 2
$Z_{analytic\_G\_dd} = Z_{analytic\_G\_qq} =$ (3.386e05*s + 8.211e08)/(s^2 + 2573*s + 3.335e08)	$Z_{analytic\_G\_dd} = Z_{analytic\_G\_qq} =$ (2.071e05*s + 6.504e07)/(s^2 + 390.9*s + 3.983e07)
$Z_{analytic\_G\_dq} = -Z_{analytic\_G\_qd} =$ (1.057e08*s^2 + 6.498e11*s - 3.473e16)/(s^4 + 1.154e04*s^3 + 7.134e08*s^2 + 3.901e12*s + 1.188e17)	$Z_{analytic\_G\_dq} = -Z_{analytic\_G\_qd} =$ (6.723e07*s^2 + 5.083e10*s - 2.339e15)/(s^4 + 4442*s^3 + 8.158e07*s^2 + 1.791e11*s + 1.61e15)

The identified parametric impedances obtained by the WSI tool in LabVIEW and used for the stability analysis are the followings.

Grid Impedance – Case 1	Grid Impedance – Case 2
$Z_{param\_G\_dd} =$ (-24.3e03 + 777.9e06*s + 328.1e03*s^2)/(3.9e06 + 333.6e06*s + 2.7e03*s^2 +1.0e0*s^3)	$Z_{param\_G\_dd} =$ (59.7e06 + 200.9e03*s)/(40.3e06 + 347.2e0*s + 1.0e0*s^2)
$Z_{paramc\_G\_qq} =$ (5.6e03 + 783.7e06*s +328.5e03*s^2)/(125.7e03 +333.5e06*s +2.7e03*s^2 +1.0e0*s^3)	$Z_{param\_G\_qq} =$ (53.9e06 + 208.9e03*s)/(40.2e06 + 358.7e0*s + 1.0e0*s^2)
Inverter in Current Mode	
$Z_{param\_S\_dd} =$ (946.1e09 + 125.5e06*s +16.5e03*s^2)/(32.7e09 + 76.7e06*s + 7.3e03*s^2 +1.0e0*s^3)	
$Z_{param\_S\_qq} =$ (505.0e09 + 89.2e06*s +17.6e03*s^2)/(17.2e09 + 41.3e06*s +6.2e03*s^2 +1.0e0*s^3)	

ACKNOWLEDGMENT

This work is supported by the European Union's Horizon 2020 research and innovation programme under grant agreement No 727481.

REFERENCES

[1] M. Liserre, T. Sauter and J. Y. Hung, "Future Energy Systems: Integrating Renewable Energy Sources into the Smart Power Grid Through Industrial Electronics," in *IEEE Industrial Electronics Magazine*, vol. 4, no. 1, pp. 18-37, March 2010

[2] D. Bogdanov, O. Koskinen, A. Aghahosseini and C. Breyer, "Integrated renewable energy based power system for Europe, Eurasia and MENA regions," *2016 International Energy and Sustainability Conference (IESC)*, Cologne, 2016, pp. 1-9

[3] B. K. Bose, "Global Energy Scenario and Impact of Power Electronics in 21st Century," in *IEEE Transactions on Industrial Electronics*, vol. 60, no. 7, pp. 2638-2651, July 2013

[4] T. Guillod, F. Krismer and J. W. Kolar, "Protection of MV Converters in the Grid: The Case of MV/LV Solid-State Transformers," in *IEEE Journal of Emerging and Selected Topics in Power Electronics*, vol. 5, no. 1, pp. 393-408, March 2017

[5] J. Sun, "Impedance-Based Stability Criterion for Grid-Connected Inverters," in IEEE Transactions on Power Electronics, vol. 26, no. 11, pp. 3075-3078, Nov. 2011

[6] Z. Bing, K. J. Karimi and J. Sun, "Input Impedance Modeling and Analysis of Line-Commutated Rectifiers," in IEEE Transactions on Power Electronics, vol. 24, no. 10, pp. 2338-2346, Oct. 2009

[7] M. Liserre, R. Teodorescu and F. Blaabjerg, "Stability of photovoltaic and wind turbine grid-connected inverters for a large set of grid impedance values," in IEEE Transactions on Power Electronics, vol. 21, no. 1, pp. 263-272, Jan. 2006

[8] B. Wen, D. Boroyevich, R. Burgos, P. Mattavelli and Z. Shen, "Analysis of D-Q Small-Signal Impedance of Grid-Tied Inverters," in IEEE Transactions on Power Electronics, vol. 31, no. 1, pp. 675-687, Jan. 2016

[9] B. Wen, D. Boroyevich, R. Burgos, P. Mattavelli and Z. Shen, "Small-Signal Stability Analysis of Three-Phase AC Systems in the Presence of Constant Power Loads Based on Measured d-q Frame Impedances," in IEEE Transactions on Power Electronics, vol. 30, no. 10, pp. 5952-5963, Oct. 2015

[10] B. Wen, D. Boroyevich, R. Burgos, P. Mattavelli and Z. Shen, "D-Q impedance specification for balanced three-phase AC distributed power system," *2015 IEEE Applied Power Electronics Conference and Exposition (APEC)*, Charlotte, NC, 2015, pp. 2757-2771

[11] B. Wen, D. Boroyevich, R. Burgos, P. Mattavelli and Z. Shen, "Inverse Nyquist Stability Criterion for Grid-Tied Inverters," in *IEEE Transactions on Power Electronics*, vol. 32, no. 2, pp. 1548-1556, Feb. 2017

[12] Middlebrook, R.D., "Input Filter Considerations in Design and Application of Switching Regulators," IEEE IAS Annual Meeting, 1976

[13] A. Riccobono and E. Santi, "Comprehensive Review of Stability Criteria for DC Power Distribution Systems," in *IEEE Transactions on Industry Applications*, vol. 50, no. 5, pp. 3525-3535, Sept.-Oct. 2014

[14] B. Miao, R. Zane, and D. Maksimovic, "System Identification of Power Converters With Digital Control Through Cross-Correlation Methods," IEEE Trans. Power Electron, vol. 20, no. 5, pp. 1093–1099, 2005

[15] A. Barkley and E. Santi, "Online Monitoring of Network Impedances Using Digital Network Analyzer Techniques," *Applied Power Electronics Conference and Exposition, 2009. APEC 2009. Twenty-Fourth Annual IEEE*, Washington, DC, 2009, pp. 440-446

[16] D. Martin, E. Santi, and A. Barkley, "Wide bandwidth system identification of AC system impedances by applying pertubations to an existing converter," Energy Conversion Congress and Exposition (ECCE), 2011 IEEE, vol., no., pp.2549,2556, 17-22 Sept. 2011

[17] D. Martin, I. Nam, J. Siegers, and E. Santi, "Wide bandwidth three-phase impedance identification using existing power electronics inverter," Applied Power Electronics Conference and Exposition (APEC), 2013 Twenty-Eighth Annual IEEE, vol., no., pp. 334,341, 17-21 March 2013

[18] A. Riccobono, S. K. A. Naqvi, A. Monti, T. Caldognetto, J. Siegers, and E. Santi, "Online wideband identification of single-phase AC power grid impedances using an existing grid-tied power electronic inverter," Power Electronics for Distributed Generation Systems (PEDG), 2015 IEEE 6th International Symposium on, vol., no., pp.1-8, 22-25 June 2015

[19] A. Riccobono, E. Liegmann, A. Monti, F. Castelli Dezza, J. Siegers and E. Santi, "Online wideband identification of three-phase AC power grid impedances using an existing grid-tied power electronic inverter," *2016 IEEE 17th Workshop on Control and Modeling for Power Electronics (COMPEL)*, Trondheim, 2016, pp. 1-8

[20] A. Riccobono, E. Liegmann, M. Pau, F. Ponci and A. Monti, "Online Parametric Identification of Power Impedances to Improve Stability and Accuracy of Power Hardware-in-the-Loop Simulations," in *IEEE Transactions on Instrumentation and Measurement*, vol. 66, no. 9, pp. 2247-2257, Sept. 2017

[21] T. Roinila, T. Messo and A. Aapro, "Impedance measurement of three phase systems in DQ-domain: Applying MIMO-identification techniques," *2016 IEEE Energy Conversion Congress and Exposition (ECCE)*, Milwaukee, WI, 2016, pp. 1-6

[22] T. Roinila, M. Vilkko and J. Sun, "Broadband methods for online grid impedance measurement," *2013 IEEE Energy Conversion Congress and Exposition*, Denver, CO, 2013, pp. 3003-3010

[23] J. Huang, K. A. Corzine and M. Belkhayat, "Small-Signal Impedance Measurement of Power-Electronics-Based AC Power Systems Using Line-to-Line Current Injection," in IEEE Transactions on Power Electronics, vol. 24, no. 2, pp. 445-455, Feb. 2009

[24] M. Jaksic, Z. Shen, I. Cvetkovic, D. Boroyevich, R. Burgos and P. Mattavelli, "Wide-bandwidth Identification of small-signal dq impedances of ac power systems via single-phase series voltage injection," *Power Electronics and Applications (EPE'15 ECCE-Europe), 2015 17th European Conference on*, Geneva, 2015, pp. 1-10

[25] Z. Staroszczyk, "A method for real-time, wide-band identification of the source impedance in power systems," in *IEEE Trans. on Instrumentation and Measurement*, vol. 54, no. 1, pp. 377-385, Feb. 2005

[26] R. Stiegler, J. Meyer, P. Schegner, and D. Chakravorty, "Measurement of network harmonic impedance in presence of electronic equipment," Applied Measurements for Power Systems (AMPS), 2015 IEEE International Workshop on, vol., no., pp. 49-54, 23-25 Sept. 2015

[27] L. Jessen and F. W. Fuchs, "Modeling of inverter output impedance for stability analysis in combination with measured grid impedances," 2015 IEEE 6th International Symposium on Power Electronics for Distributed Generation Systems (PEDG), Aachen, 2015, pp. 1-7

[28] Jessen, L.; Gunter, S.; Fuchs, F.W.; Gottschalk, M.; Hinrichs, H.-J., "Measurement results and performance analysis of the grid impedance in different low voltage grids for a wide frequency band to support grid integration of renewables," in Energy Conversion Congress and Exposition (ECCE), 2015 IEEE , vol., no., pp.1960-1967, 20-24 Sept. 2015

[29] T. T. Do, M. Jordan, H. Langkowski, and D. Schulz, " Novel Grid Impedance Measurement Setups in Electrical Power Systems," Applied Measurements for Power Systems (AMPS), 2016 IEEE International Workshop on, 28-30 Sept. 2016

[30] Sumner, M.; Palethorpe, B.; Thomas, D.W.P.; Zanchetta, P.; Di Piazza, M.C., "A technique for power supply harmonic impedance estimation using a controlled voltage disturbance," Power Electronics, IEEE Transactions on , vol.17, no.2, pp.207,215, Mar 2002

[31] G. Francis, R. Burgos, D. Boroyevich, F. Wang and K. Karimi, "An algorithm and implementation system for measuring impedance in the D-Q domain," *2011 IEEE Energy Conversion Congress and Exposition*, Phoenix, AZ, 2011, pp. 3221-3228

[32] L. Ljung, System Identification: Theory for the User, 2nd ed. Englewood Cliffs, NJ: Prentice-Hall, 1999

[33] J. Duncan Glover, Power System Analysis and Design, 5th ed. Cengage Learning, 2012

[34] http://www.opal-rt.com/sites/default/files/OP5600%20Simulator%20User%20Manual.pdf

[35] http://sine.ni.com/nips/cds/view/p/lang/en/nid/207368

[36] J. Wang, N. C. P. Chang, X. Feng and A. Monti, "Design of a Generalized Control Algorithm for Parallel Inverters for Smooth Microgrid Transition Operation," in *IEEE Transactions on Industrial Electronics*, vol. 62, no. 8, pp. 4900-4914, Aug. 2015

[37] R. W. Erickson and D. Maksimovic, Fundamentals of power electronics, 2nd ed. Norwell, MA: Kluwer Academic, 2001

[38] Understanding FFTs and Windowing, White Paper available at http://www.ni.com/white-paper/4844/en/

[39] OPAL-RT: "RT-Events 4.0 – Block Library Reference Guide". Available: http://www.opal-rt.com/download-center/

[40] Riccobono and E. Santi, "Positive Feedforward Control of Three-Phase Voltage Source Inverter for DC Input Bus Stabilization With Experimental Validation," in IEEE Transactions on Industry Applications, vol. 49, no. 1, pp. 168-177, Jan.-Feb. 2013

[41] R. Burgos, D. Boroyevich, F. Wang, K. Karimi and G. Francis, "On the Ac stability of high power factor three-phase rectifiers," *2010 IEEE Energy Conversion Congress and Exposition*, Atlanta, GA, 2010, pp. 2047-2054

[42] B. Wen, D. Boroyevich, R. Burgos and P. Mattavelli, "c," *2014 IEEE Energy Conversion Congress and Exposition (ECCE)*, Pittsburgh, PA, 2014, pp. 163-169

[43] https://de.mathworks.com/help/mpc/gs/using-simulink-to-develop-lti-models.html

[44] E. C. Levy, "Complex-curve fitting," in IRE Transactions on Automatic Control, vol. AC-4, no. 1, pp. 37-43, May 1959

[45] L. Harnefors, "Modeling of Three-Phase Dynamic Systems Using Complex Transfer Functions and Transfer Matrices," in *IEEE Transactions on Industrial Electronics*, vol. 54, no. 4, pp. 2239-2248, Aug. 2007.

[46] J. Sun, "Small-Signal Methods for AC Distributed Power Systems–A Review," in IEEE Transactions on Power Electronics, vol. 24, no. 11, pp. 2545-2554, Nov. 2009

[47] M. Cespedes and J. Sun, "Impedance Modeling and Analysis of Grid-Connected Voltage-Source Converters," in IEEE Transactions on Power Electronics, vol. 29, no. 3, pp. 1254-1261, March 2014

[48] Roinila T., Vilkko M., Sun J., Online Grid Impedance Measurement Using Discrete-Interval Binary Sequence Injection, IEEE Journ. of Emerg. and Select. Topics in Power Electr., Vol 2, Issue 4, pp 985-993, 2014